

# HERSCHEL\* FAR-INFRARED SPECTRAL-MAPPING OF ORION BN/KL OUTFLOWS: SPATIAL DISTRIBUTION OF EXCITED CO, H<sub>2</sub>O, OH, O AND C<sup>+</sup> IN SHOCKED GAS

JAVIER R. GOICOECHEA<sup>1,2</sup>, LUIS CHAVARRÍA<sup>2,3</sup>, JOSÉ CERNICHAÑO<sup>1,2</sup>, DAVID A. NEUFELD<sup>4</sup>,  
ROLAND VAVREK<sup>5</sup>, EDWIN A. BERGIN<sup>6</sup>, SARA CUADRADO<sup>1,2</sup>, PIERRE ENCRENAZ<sup>7</sup>,  
MIREYA ETXALUZE<sup>1,2</sup>, GARY J. MELNICK<sup>8</sup>, EDWARD POLEHAMPTON<sup>9,10</sup>

*Accepted for publication in Astrophysical Journal. November 11, 2014*

## ABSTRACT

We present  $\sim 2' \times 2'$  spectral-maps of Orion BN/KL outflows taken with *Herschel* at  $\sim 12''$  resolution. For the first time in the far-IR domain, we spatially resolve the emission associated with the bright H<sub>2</sub> shocked regions “Peak 1” and “Peak 2” from that of the Hot Core and ambient cloud. We analyze the  $\sim 54\text{--}310\ \mu\text{m}$  spectra taken with the PACS and SPIRE spectrometers. More than 100 lines are detected, most of them rotationally excited lines of <sup>12</sup>CO (up to  $J=48\text{--}47$ ), H<sub>2</sub>O, OH, <sup>13</sup>CO, and HCN. Peaks 1/2 are characterized by a very high  $L(\text{CO})/L_{\text{FIR}} \approx 5 \times 10^{-3}$  ratio and a plethora of far-IR H<sub>2</sub>O emission lines. The high- $J$  CO and OH lines are a factor  $\approx 2$  brighter toward Peak 1 whereas several excited H<sub>2</sub>O lines are  $\lesssim 50\%$  brighter toward Peak 2. Most of the CO column density arises from  $T_k \sim 200\text{--}500\text{ K}$  gas that we associate with low-velocity shocks that fail to sputter grain ice mantles and show a maximum gas-phase H<sub>2</sub>O/CO  $\lesssim 10^{-2}$  abundance ratio. In addition, the very excited CO ( $J>35$ ) and H<sub>2</sub>O lines reveal a hotter gas component ( $T_k \sim 2500\text{ K}$ ) from faster ( $v_s > 25\text{ km s}^{-1}$ ) shocks that are able to sputter the frozen-out H<sub>2</sub>O and lead to high H<sub>2</sub>O/CO  $\gtrsim 1$  abundance ratios. The H<sub>2</sub>O and OH luminosities cannot be reproduced by shock models that assume high (undepleted) abundances of atomic oxygen in the preshock gas and/or neglect the presence of UV radiation in the postshock gas. Although massive outflows are a common feature in other massive star-forming cores, Orion BN/KL seems more peculiar because of its higher molecular luminosities and strong outflows caused by a recent explosive event.

*Subject headings:* stars: protostars ISM: jets and outflows infrared: ISM shock waves

## 1. INTRODUCTION

The Becklin-Neugebauer/Kleinmann-Low (BN/KL) region at the core of the Orion molecular cloud 1 (OMC1) and behind the Orion Nebula stellar cluster (Genzel & Stutzki 1989; O’dell 2001) is the nearest ( $\sim 414\text{ pc}$ ) and probably the most studied high-mass star-forming region (Menten & Reid 1995; Reid et al. 2007). In addition to source BN, two more compact H II sources separated by  $\sim 3''$  are known to exist at the centre of Orion BN/KL, sources *I* and *n*. The 3 sources are within a region of

$\sim 10''$  ( $\sim 0.02\text{ pc}$ ). Their proper motions reveal that they run away from a common region, suggesting that BN, *I*, and *n* were originally part of a multiple protostellar system that merged  $\lesssim 1000$  years ago (Bally & Zinnecker 2005; Gómez et al. 2005; Zapata et al. 2009; Bally et al. 2011; Peng et al. 2012a; Nissen et al. 2012). The consequences of such an explosive event are likely related to the high-velocity CO emission and the bright, wide-angle H<sub>2</sub> outflow observed in the region since the late 70’s (e.g., Kwan & Scoville 1976; Beckwith et al. 1978).

The different physical conditions and velocity fields along the line of sight however, complicate the interpretation of Orion BN/KL observations. This is especially true for the low angular resolution observations carried out with single-dish telescopes. For this reason, it is common to distinguish between different physical components in the region (see Blake et al. 1987; Tercero et al. 2010): the “ridge” (extended quiescent molecular gas), the “Hot Core” (a collection of very dense and hot clumps showing an extremely rich chemistry), and the “plateau” (a mixture of outflows, shocks, and interactions with the ambient cloud).

Different supersonic molecular outflows arise from the core of Orion BN/KL. A low-velocity outflow expanding at  $\sim 18\text{ km s}^{-1}$  and showing a northeast-southwest (NE-SW) orientation was inferred from the proper motions of H<sub>2</sub>O masers (e.g., Genzel et al. 1981) and is thought to be driven by source *I* (Beuther & Nissen 2008). More recent interferometric observations of the <sup>13</sup>CO  $J=2\text{--}1$  line suggest the presence of a roughly spherical bubble expanding at  $\sim 15\text{ km s}^{-1}$  and with its center of symmetry

jr.goicoechea@icmm.csic.es

\* *Herschel* is an ESA space observatory with science instruments provided by European-led Principal Investigator consortia and with important participation from NASA.

<sup>1</sup> Instituto de Ciencia de Materiales de Madrid (ICMM-CSIC). Sor Juana Ines de la Cruz 3, 28049 Cantoblanco, Madrid, Spain.

<sup>2</sup> Centro de Astrobiología, CSIC-INTA, Ctra. de Torrejón a Ajalvir km 4, E-28850 Madrid, Spain.

<sup>3</sup> Universidad de Chile/CONICYT, Camino del Observatorio 1515, Las Condes, Santiago, Chile.

<sup>4</sup> Department of Physics & Astronomy, Johns Hopkins University 3400 North Charles Street, Baltimore, MD 21218, USA

<sup>5</sup> Herschel Science Center, ESA/ESAC, P.O. Box 78, Villanueva de la Cañada, E-28691 Madrid, Spain

<sup>6</sup> Department of Astronomy, University of Michigan, 500 Church Street, Ann Arbor, MI, 48109, USA

<sup>7</sup> LERMA, UMR 8112 du CNRS, Observatoire de Paris, École Normale Supérieure, France

<sup>8</sup> Harvard-Smithsonian Center for Astrophysics, 60 Garden Street, MS 66, Cambridge, MA 02138, USA

<sup>9</sup> RAL Space, Rutherford Appleton Laboratory, Chilton, Didcot, Oxfordshire OX11 0QX, UK

<sup>10</sup> Institute for Space Imaging Science, University of Lethbridge, 4401 University Drive, Lethbridge, Alberta T1J 1B1, Canada

coinciding with the region where the protostellar system presumably merged, the “explosion center” (Zapata et al. 2011). On the other hand, an even more powerful, but less understood, wide-angle high-velocity outflow, expanding at  $\sim 30 \text{ km s}^{-1}$  to a hundred  $\text{km s}^{-1}$  exists and shows a northwest-southeast (NW-SE) orientation approximately perpendicular to the low-velocity outflow (e.g., Allen & Burton 1993; O’dell 2001). The high-velocity outflow contains the two brightest infrared  $\text{H}_2$  emission peaks in the sky: Peak 1 and Peak 2 (Beckwith et al. 1978), with a total  $\text{H}_2$  line luminosity of  $120 \pm 60 L_{\odot}$  (Rosenthal et al. 2000) and extending over a  $\sim 2' \times 2'$  area. The  $\text{H}_2$  Peak 1 is located  $\sim 30''$  NW of the Hot Core, and is the brightest  $\text{H}_2$  lobe of the wide-angle outflow. Peak 2 is  $\sim 20''$  SE of the Hot Core. A detailed analysis of the  $\text{H}_2$  ro-vibrational line emission toward Peak 1 shows excitation temperatures increasing from  $\sim 600 \text{ K}$  to about  $3200 \text{ K}$  (Rosenthal et al. 2000). Such extreme conditions are consistent with shock-excited material as the outflow(s) plunge into the ambient cloud, heating and compressing the molecular gas to high temperatures and densities.

Ground-based observations of the high-speed CO  $J=2-1$  bullets (Rodríguez-Franco et al. 1999; Zapata et al. 2009) and of the  $J=6-5$  and  $7-6$  high-velocity emission (Peng et al. 2012a; 2012b) correlate with the  $\text{H}_2$  fingers seen in the near-IR, thus suggesting a common origin. Therefore, in addition to being an excellent laboratory for star formation theories, the environment around Orion BN/KL, the  $\text{H}_2$  Peaks in particular, are among the closest and brightest regions to study the properties and processing of interstellar material by shock waves.

Early models of interstellar shocks in molecular clouds already predicted that, depending on their nature and on the strength and orientation of the magnetic field, they will radiate high luminosities of molecular line emission ( $\text{H}_2$ ,  $\text{H}_2\text{O}$  and CO in particular, see e.g., Hollenbach & McKee 1979; Draine et al. 1983; Kaufman & Neufeld 1996; Bergin et al. 1998). Unfortunately, while the  $\text{H}_2$ , CO and  $\text{H}_2\text{O}$  vibrational spectrum can be observed toward sources of relatively low extinction (see e.g., Rosenthal et al. 2000; González-Alfonso et al. 2002, for mid-IR observations toward Peak 1), the relevant  $\text{H}_2\text{O}$ , CO and OH rotational lines appear at far-IR wavelengths that can only be observed from airborne or space telescopes. In particular, the water abundance and its role in the cooling of the warm interstellar gas has been a pivotal problem in any discussion about molecular shocks (see van Dishoeck et al. 2013, for a comprehensive review).

The *Kuiper Airborne Observatory* (KAO) and the *Infrared Space Observatory* (ISO) opened the far-IR sky to spectroscopic observations. The [OI] fine structure lines, and the high- $J$  CO,  $\text{H}_2\text{O}$  and OH rotational lines were first detected toward Orion BN/KL and other star-forming regions revealing shock-excited material in many interstellar environments (e.g., Genzel & Stutzki 1989; Schmid-Burgk et al. 1989; van Dishoeck 2004; Cernicharo & Crovisier 2005). Unfortunately, the small aperture of KAO and ISO greatly limited the sensitivity and the spatial resolution of those pioneering observations even toward nearby regions like Orion. The much higher angular and spectral capabilities provided by *Herschel* 3.5 m space telescope (Pilbratt et al. 2010) allowed us to carry out a broadband spectral-mapping of the  $\sim 2' \times 2'$

region around Orion BN/KL. For the first time at these wavelengths, we can separate the emission from the shock-excited  $\text{H}_2$  Peaks from that of the central Hot Core regions where most (sub)mm molecular lines peak. The Orion  $\text{H}_2$  Peaks 1/2 are unique templates of a shock-excited environment where a significant fraction of the gas cooling is due to far-IR lines. In this work, we spatially resolve the emission from all relevant far-IR cooling lines with an unprecedented  $\sim 12''$  ( $\simeq 5000 \text{ AU}$ ) resolution.

The spectral-maps presented here were taken with the PACS spectrometer (Poglitsch et al. 2010) as a part of the HEXOS GT Key Program, *Herschel observations of EXtra-Ordinary Sources* (Bergin et al. 2010). They were complemented with SPIRE-FTS (Griffin et al. 2010) observations toward Orion BN/KL. The paper is organized as follows. In Section 2 we present the data set and the data reduction technique. In Section 3 we show the spatial distribution of CO,  $\text{H}_2\text{O}$ , OH and the atomic fine structure lines in the region and also describe the nearly complete  $\sim 54\text{--}310 \mu\text{m}$  spectrum toward  $\text{H}_2$  Peak 1/2. In Section 4 we analyze maps of different line surface brightness ratios, construct CO,  $\text{H}_2\text{O}$  and OH rotational diagrams and present a simple non-LTE model of the far-IR line emission toward Peak 1. In Section 5 we examine the line cooling in the region and in Section 6 we discuss our results in the context of shock models available in the literature. We finally compare our observations with those toward more distant high-mass star-forming cores.

## 2. OBSERVATIONS AND DATA REDUCTION

### 2.1. Non-standard PACS observations of BN/KL core

The PACS spectrometer was used to observe the core of Orion BN/KL at wavelengths between  $\sim 54$  and  $\sim 190 \mu\text{m}$ . PACS used photoconductor detectors providing 25 spectra over a  $47'' \times 47''$  field of view (FoV) and resolved  $5 \times 5$  “spaxels”, each with a size of  $9.4'' \times 9.4''$  in the sky. The resolving power varies between  $R \sim 1000\text{--}1500$  ( $\sim 108\text{--}190 \mu\text{m}$  range),  $\sim 1700\text{--}3000$  ( $70\text{--}94 \mu\text{m}$  range) and  $\sim 2700\text{--}5500$  ( $54\text{--}70 \mu\text{m}$  range). The measured width of the PACS spectrometer point spread function (PSF) is relatively constant for  $\lambda \lesssim 100 \mu\text{m}$  ( $\simeq$  spaxel size) but increases at longer wavelengths. In particular only between  $\sim 74\%$  and  $41\%$  of a point source emission would fall in a given spaxel between  $\sim 54$  and  $190 \mu\text{m}$ .

Owing to the very high far-IR continuum levels expected in the core of BN/KL (above the standard saturation limits of PACS) these observations were conducted in a specific *non-standard* engineering observing mode (*PacsCalWaveCalNoChopBurst*). In particular, the detector capacitances and the integration ramp lengths per grating scan were modified from their standard values according to the expected continuum fluxes. Single-pointing observations with the PACS array were carried out in April 2011 using the “unchopped” mode. The PACS array was centered at  $\alpha_{2000}: 5^{\text{h}}35^{\text{m}}14.5^{\text{s}}$ ,  $\delta_{2000}: -5^{\circ}22'30.9''$  in the Hot Core region (ObsIDs 1342218575 and 1342218576). We checked that the observations were not affected by the decrease of temperature of the star-tracker camera during orbits 320 and 761 and thus the pointing is accurate within  $\sim 2''$ . Background subtraction was achieved by removing the telescope spectrum measured on a distant reference OFF-

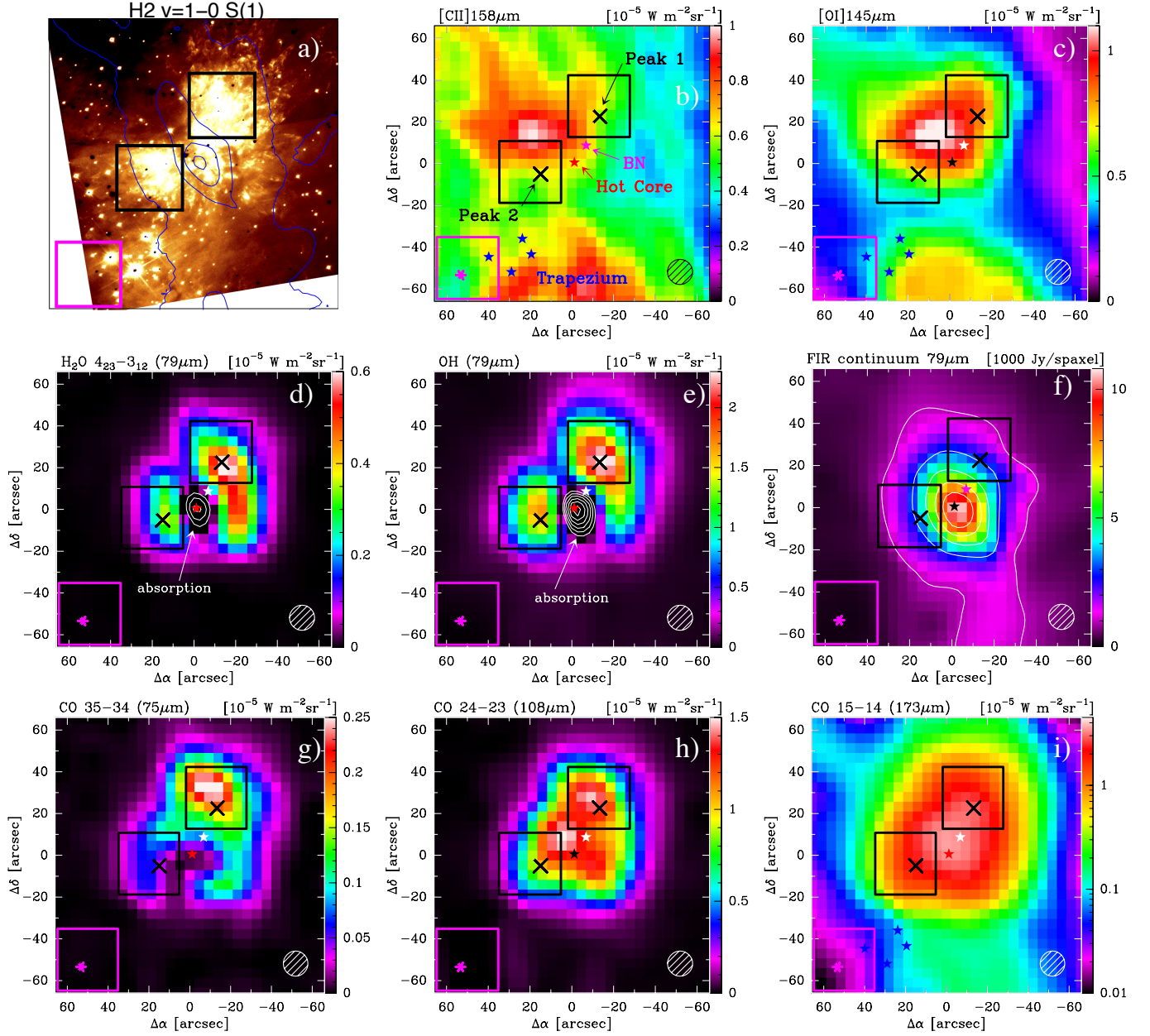


**Figure 1.** Line surface brightness maps obtained with *Herschel*/PACS toward Orion BN/KL. The FoV is  $2' \times 2'$ . The areas used to compute the line luminosities in the three representative regions discussed in the text (Peak 1, Peak 2 and ambient cloud) are shown with black and pink squares respectively. The black crosses and the pink star show the exact positions where the spectra shown in Figure 2 are extracted. The position of the BN source and that of the Orion Hot core are also shown in each panel as colored stars. Panel a) H<sub>2</sub> emission distribution in the region (Bally et al. 2011). The 4 blue contours show the SCUBA 450  $\mu$ m continuum emission at 3 $\sigma$  and 20, 50 and 90% of the emission peak respectively Johnstone & Bally (1999). Panel b) shows the [C II] 158  $\mu$ m line surface brightness. The position of the Trapezium stars are marked with blue stars. The white contours in panels d) and e) represent H<sub>2</sub>O and OH line absorption contours toward the FIR continuum peak (from  $-0.1 \times 10^{-5}$  to  $-0.4 \times 10^{-5}$  W m<sup>-2</sup> sr<sup>-1</sup> in steps of  $0.1 \times 10^{-5}$  W m<sup>-2</sup> sr<sup>-1</sup> for o-H<sub>2</sub>O 4<sub>23</sub>-3<sub>12</sub>, and from  $-0.1 \times 10^{-5}$  to  $-1.1 \times 10^{-5}$  W m<sup>-2</sup> sr<sup>-1</sup> in steps of  $0.2 \times 10^{-5}$  W m<sup>-2</sup> sr<sup>-1</sup> for OH  $^2\Pi_{1/2}$ - $^2\Pi_{3/2}$   $J=1/2$ -3/2). Outside this region, lines are observed in emission. Panel f) shows the strong FIR continuum emission distribution at 79  $\mu$ m measured by the PACS spectrometer. Panels g), h) and i) show how the far-IR CO emission peak shifts toward Peak 1 as the  $J$  rotational number increases and the observed wavelength decreases. The  $\sim 12''$  angular resolution is shown in the bottom-right corner of each panel.

position separated by  $\sim 20'$  in right ascension. Reference observations (ObsIDs 1342218573, 1342218574, 1342218577 and 1342218578) were carried out before and after the ON-source observations. The total observing time was 2.2h. The resulting data were indeed above the standard PACS saturation limits, with continuum flux densities above  $13000 \text{ Jy spaxel}^{-1}$  in the R1 grating order. The response drifts due to self-curing were estimated to be within  $\sim 15\%$ , otherwise the data looked fine and were validated for further scientific analysis.

### 2.2. PACS $2' \times 2'$ spectral maps

The PACS spectrometer was also used to map the  $\sim 2' \times 2'$  region encompassing the Orion BN/KL outflows in the 70-94 and 108-190  $\mu\text{m}$  ranges (B2B and R1 grating orders respectively). Nine individual pointings of the PACS array were done to cover the region in a  $3 \times 3$  raster map with a step of one PACS FoV.

Mapping observations were carried out in April 2011 using the range spectroscopy “unchopped” mode. The map was also centered at the Hot Core position (ObsID 1342218572). Background subtraction was achieved by removing the telescope spectrum measured on the same reference OFF-position (ObsID 1342218571). The reference OFF position spectrum showed a weak  $[\text{C II}] 158 \mu\text{m}$  line emission contamination that was removed before ON-OFF subtraction. Owing to the high far-IR continuum fluxes densities expected in the region (a few thousand  $\text{Jy spaxel}^{-1}$ ), these mapping observations were conducted in the *standard mode* but using the maximum capacitance allowed by the PACS detectors. Still, the data below  $\sim 130 \mu\text{m}$  were saturated in the 25 spaxels of the central PACS array pointing. These spectra were substituted by the *non-standard* data discussed in Sect. 2.1. The total mapping observing time was  $\sim 3.4$  h.

### 2.3. Line flux extraction

PACS data were processed using version 8 of the Herschel Interactive Processing Environment (HIPE) and then exported to GILDAS where basic line spectrum manipulations were carried out. The PACS flux calibration accuracy is limited by detector response drifts and slight pointing offsets. The absolute flux calibration accuracy is determined by observations of 30 standard flux calibrators carried out by the PACS instrument team and is estimated to be of the order of  $\pm 30\%$ <sup>12</sup>. Additional processing of the spectral-maps was carried out using dedicated *fortran90* subroutines. In particular, the raster map spectra were gridded to a regular data cube through convolution with a Gaussian kernel. The final angular resolution in the maps is  $\sim 12''$ . Figure 1 shows a selection of PACS line and continuum maps and Figure 2 shows high signal-to-noise (S/N) spectra toward the  $(-13'', +23'')$  position in the Peak 1 region (black histograms) and toward the  $(+55'', -53'')$  position in the ambient cloud (pink histograms in panels 2a and 2b). Panels 2c, 2d and 2e show the shortest-wavelength spectra toward Peak 1 again (black) and toward the  $(+19'', -4'')$  position in the Peak 2 region (gray).

Our PACS maps are not fully sampled spatially and the individual spaxels do not fill the PSF entirely. For semi-

extended sources this means that accurate line surface brightness can only be extracted adding the fluxes measured in apertures that cover several spaxels. The black and pink squares in Figure 1 show the  $\sim 30'' \times 30''$  areas used to extract the line fluxes between 70 and 190  $\mu\text{m}$  in the Peak 1/2 regions and in the ambient cloud. A third aperture around the  $(0'', 0'')$  map position was defined to extract the CO line fluxes in the Hot Core region. Only for lines in the 54-70  $\mu\text{m}$  range (not mapped), line fluxes toward Peaks 1/2 were directly extracted from the  $(-13'', +23'')$  and  $(+19'', -4'')$  spaxels (*non-standard* observations in Sect. 2.1) and then calibrated using the PACS point source correction. Owing to the almost constant PSF width at these short wavelengths, the resulting line intensities are in good agreement (below the absolute calibration accuracy) with those expected at longer wavelengths and extracted from the maps. Lines in the PACS wavelength ranges affected by detector leakage were not included in the analysis.

### 2.4. SPIRE FTS maps

SPIRE FTS spectra between  $\sim 194$  and  $\sim 671 \mu\text{m}$  (1545-447 GHz) were obtained on March 2011 in the high spectral resolution mode ( $\Delta\lambda = 0.04 \text{ cm}^{-1}$ ). The SPIRE FTS uses two bolometer arrays covering the 194-310  $\mu\text{m}$  (Short Wavelength array, SSW) and 303-671  $\mu\text{m}$  (Long Wavelength array, SLW) bands. The two arrays contain 19 (SLW) and 37 (SSW) hexagonally packed detectors separated by  $\sim 2$  beams ( $51''$  and  $33''$  respectively). The unvignetted FoV is  $\sim 2'$ . The SPIRE FTS observation (ObsID 1342216879) was centered at the same PACS map  $(0'', 0'')$  position. Observations were done in the *bright source mode*. The total observing time of the SPIRE sparse sampling map was 9 min.

Owing to the extended nature of the line emission in Orion, we applied the *extended emission* pipeline to reduce the data with HIPE 11 (Lu et al. 2013). Once reduced and calibrated, we used the unapodized spectra to fit the line intensities using sinc functions. Opposite to PACS, the SPIRE pipeline provides the line surface brightnesses directly in  $\text{W m}^{-2} \text{ sr}^{-1}$ . We checked that the CO  $J=13-12$  line intensities toward Peak 1, the Hot Core and the ambient cloud position agree (within  $\sim 30\%$ ) with the line intensity expected from the CO  $J=14-13$  line intensities observed by PACS and extracted in  $\sim 30'' \times 30''$  apertures. The 194-313  $\mu\text{m}$  spectra taken from the two SSW detectors pointing toward Peak 1 and the ambient position are shown in Fig. 2. The units of  $\text{Jy/beam}$  in Fig. 2 were obtained by multiplying the spectrum in  $\text{W m}^{-2} \text{ Hz}^{-1} \text{ sr}^{-1}$  by the effective beam size for extended sources (see Swinyard et al. 2014). Note that no SLW detector ( $303-671 \mu\text{m}$ ) matched the coordinates of the Peak 1 and ambient cloud positions observed with PACS thus they are not shown in Figure 2.

<sup>12</sup> PACS Spectroscopy performance and calibration, PACS/ICC document ID P1CC-KL-TN-041 (Vandenbussche et al.).

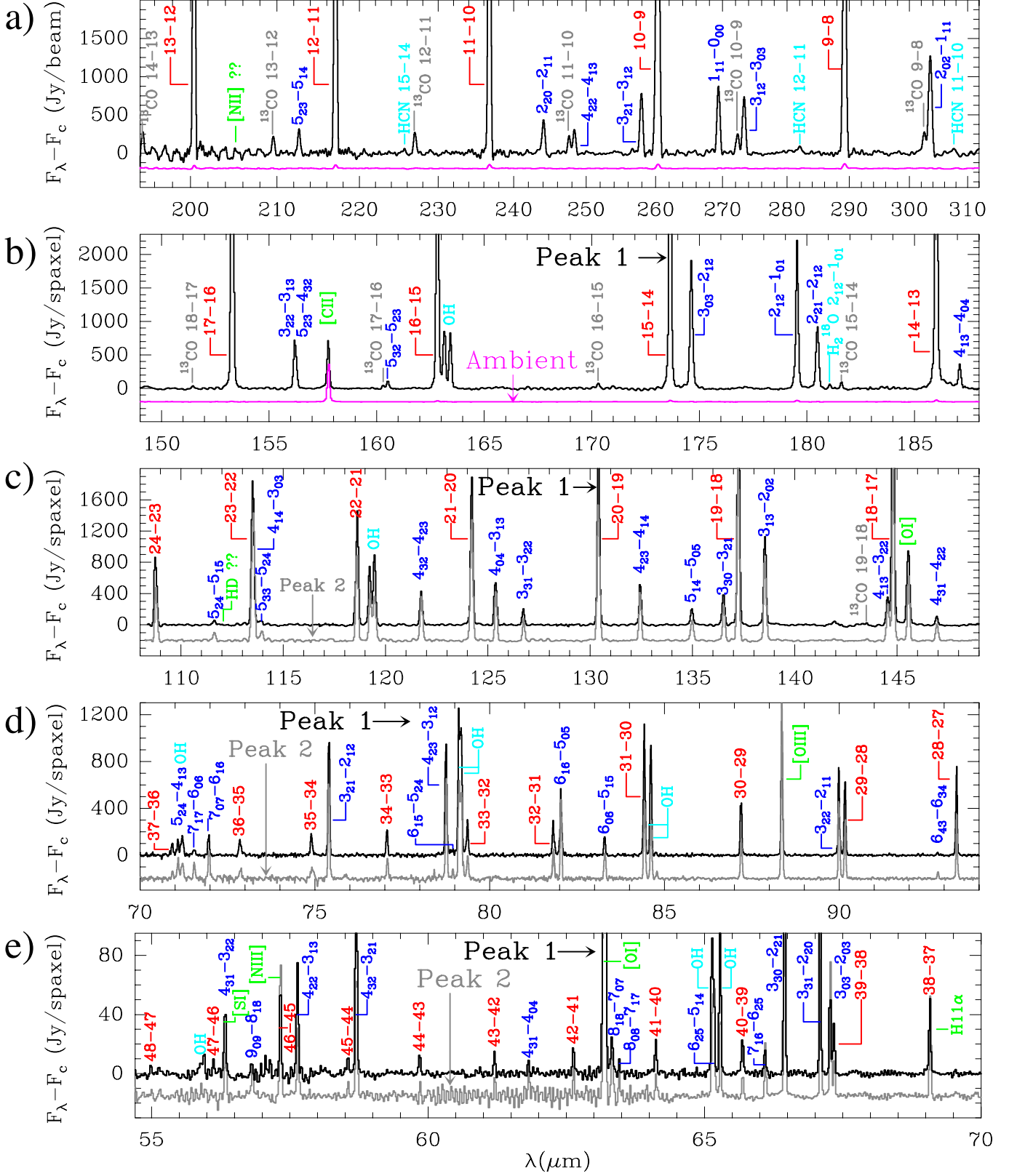


**Figure 2.** Panels a) and b): Continuum-subtracted SPIRE-FTS spectra (apodized for clarity in the figure) and PACS spectra toward Orion H<sub>2</sub> Peak 1 (black) and toward an ambient cloud position (pink) (see Figure 1). Panels c), d) and e): Continuum-subtracted PACS spectra toward Peak 1 (black) and Peak 2 (gray). Note that the ambient cloud and Peak 2 spectra are shifted to ease the comparison. Flux density units are in Jy/beam for SPIRE and Jy/spaxel and for PACS (y-axis). The x-axis shows the spectrum wavelength in microns. All detected spectral features are labelled (<sup>12</sup>CO rotational lines in red, H<sub>2</sub>O lines in blue, etc.).

### 3. RESULTS

#### 3.1. Spatial distribution of CO, H<sub>2</sub>O, OH, O and C<sup>+</sup>

Figure 1 shows a selection of  $\sim 2' \times 2'$  continuum and line surface brightness maps taken with *Herschel*/PACS. In these figures, the colored stars show the position of source BN and of the Hot Core (including the famous IRC2 source and radio sources *I* and *n*). The crosses show the positions of the vibrationally excited H<sub>2</sub> emission peaks in the region (Beckwith et al. 1978), referred as Peak 1 in the NW and Peak 2 in the SE (see Fig.1a). The far-IR dust continuum peaks at the Hot Core position. The strong continuum emitting region at  $\sim 79 \mu\text{m}$  has a radius of  $\sim 15''$  at half-maximum power and decreases outwards following the NE-SW direction along the ridge (Fig.1f).

The spatial distribution of the CO line surface brightness is not homogeneous and depends on the  $J$  rotational number. The brightest <sup>12</sup>CO lines are those between  $J=15$  and 20. They show a roughly spherical distribution, with an approximated half-power radius of  $\sim 25''$  (see Fig. 1i for the  $J=15-14$  line). The innermost regions of this spherical structure could correspond to the expanding bubble reported by Zapata et al. (2011) and falling at the center of the observed structure. The <sup>13</sup>CO  $J=16-15$  and  $15-14$  lines are less affected by opacity effects and they peak slightly NE of the Hot Core. As  $J$  increases, the CO spatial distribution changes. Figure 1h shows that the  $J=24-23$  line ( $E_u/k=1658$  K) peaks toward two different positions with similar integrated intensities, one  $\sim 10''$  NE of the Hot Core (characteristic shocks produced by the low-velocity outflows) and other  $\sim 30''$  NW in the H<sub>2</sub> Peak 1 region. Peak 1 becomes much more apparent in the very high- $J$  line emission maps (see Fig. 1g for the  $J=35-34$  line with  $E_u/k=3474$  K). Unlike other molecules emitting in the (sub)mm, the very high- $J$  <sup>12</sup>CO line surface brightness maps resemble the vibrationally excited H<sub>2</sub> images, suggesting that they trace the same high-excitation shocked gas. In fact, the very high- $J$  CO emission morphology revealed by PACS is similar to the high-velocity ( $|v_{lsr}| > 70 \text{ km s}^{-1}$ ) CO  $J=7-6$  and  $6-5$  line emission mapped with APEX (Peng et al. 2012a) and reasonably follows the spatial distribution of the high-velocity CO  $J=2-1$  bullets resolved by the SMA interferometer. Interestingly, their distribution also show an emission “hole” inside the explosion center region (Zapata et al. 2009). All together, this suggests that the much higher-energy far-IR CO lines are dominated by material moving at high speeds.

Most of the far-IR H<sub>2</sub>O and OH rotational lines are sensitive to the strength of the dust continuum field. The angular resolution of our *Herschel*/PACS maps is comparable to the half-power size of the far-IR continuum source. The very strong continuum flux from the central region makes that a significant fraction of the H<sub>2</sub>O and OH lines toward the Hot Core appear either in absorption or show P-Cygni profiles (Figure 3). These characteristic line profiles probe the expanding outflows in the region and were previously inferred from *KAO* and *ISO* observations (e.g., Melnick et al. 1990; Wright et al. 2000; Cernicharo et al. 2006; Goicoechea et al. 2006). The much higher angular resolution of *Herschel* allows us to spatially resolve the regions where these lines switch to pure emission as the far-IR continuum becomes weaker, as the

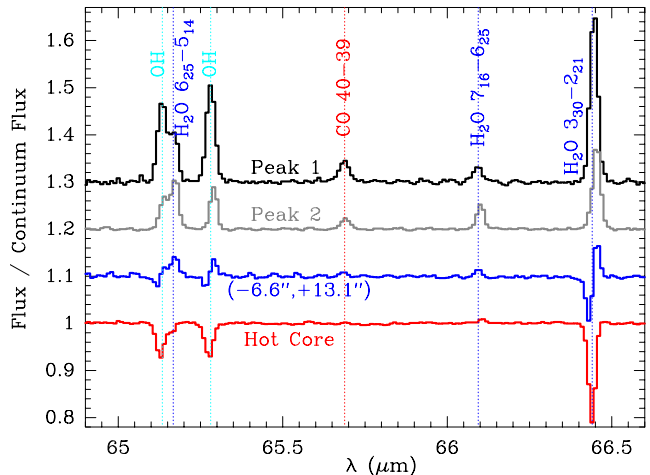


**Figure 3.** *Herschel*/PACS spectra around  $\sim 65 \mu\text{m}$  showing the evolution of H<sub>2</sub>O and OH line profiles toward Peak 1 (black), Peak 2 (gray), the Hot Core (red) and toward an intermediate position (blue). The continuum flux is very strong toward the Hot Core and decreases toward Peak 1/2 which show pure emission far-IR spectra.

gas density increases or both. Figures 1d and 1e show the spatial distribution of the *o*-H<sub>2</sub>O  $4_{23}-3_{12}$  ( $E_u/k=398$  K) and OH  $^2\Pi_{1/2}-^2\Pi_{3/2}$   $J=1/2-3/2$  ( $E_u/k=182$  K) lines at  $\sim 79 \mu\text{m}$ . Both lines show a similar spatial distribution and are representative of other H<sub>2</sub>O and OH lines, with the absorption lines peaking toward the continuum source and the emission lines showing a NW-SE distribution characteristic of the wide-angle H<sub>2</sub> outflow and peaking toward the Peak 1 and 2 regions.

The [C II]  $158 \mu\text{m}$  and [O I]  $145 \mu\text{m}$  lines have also been mapped and they show a different spatial distribution compared to molecular lines. Their emission distribution show a more NE-SW orientation with the [O I]  $145 \mu\text{m}$  line peaking  $\sim 15''$  NE from the Hot Core. The [C II]  $158 \mu\text{m}$  line shows a similar spatial distribution, but the emission toward Peak 1 and 2 is even weaker.

#### 3.2. The $\sim 54-310 \mu\text{m}$ spectrum of Orion Peak 1/2

Figure 2 shows the pure emission spectrum extracted toward Peak 1 (black histograms) and Tables A.1 to A.6 list the fluxes of all detected lines in the  $54-310 \mu\text{m}$  range. The first complete far-IR spectrum taken toward Orion BN/KL with *ISO* (Lerate et al. 2006) had a very poor angular resolution of  $\sim 80''$ , thus mixing different physical components and also mixing the emission/absorption components in the line of sight. With *Herschel* we can extract and isolate the complete far-IR spectrum toward H<sub>2</sub> Peak 1. This region is also an emission peak in the very high- $J$  CO lines ( $J > 30$ ). In the following we describe the main attributes of the far-IR spectrum toward H<sub>2</sub> Peak 1 shown in Figure 2.

More than 100 lines have been detected, most of them rotationally excited lines from abundant molecules: 34 <sup>12</sup>CO lines (up to  $J=48-47$  and  $E_u/k=6458$  K), 44 lines of both *o*-H<sub>2</sub>O and *p*-H<sub>2</sub>O (up to  $8_{26}-7_{35}$  and  $E_u/k=1414$  K), 13 OH lines (up to  $^2\Pi_{1/2}$   $J=9/2-7/2$  and  $E_u/k=876$  K), 11 <sup>13</sup>CO lines (up to  $J=19-18$  and  $E_u/k=1004$  K) and several HCN lines (up to  $J=15-14$  and  $E_u/k=510$  K). Several atomic fine structure lines are detected: [C II]  $158 \mu\text{m}$ , [O I]  $63, 145 \mu\text{m}$ , [O III]  $88 \mu\text{m}$



and [N III] 57  $\mu\text{m}$ . Note that the last two lines arise from the foreground H II region (the Orion nebula). Hence, a significant contribution of the [C II] and [O I] line emission arises from the PDR interfaces between this very extended H II region and the molecular cloud that embeds BN/KL and thus they are not be entirely related with the molecular outflows.

Approximately 10% of the observed H<sub>2</sub>O and CO emission toward Peak 1 arises from high energy transitions, with  $E_u/k > 600$  K for water vapor and  $E_u/k > 2000$  K for CO ( $J > 27$ ). Here we are specially interested in constraining the abundances and physical conditions of the material where these high excitation transitions arise.

The Peak 2 region displays a similar molecular spectrum with only small differences in the line fluxes. In particular, Peak 2 shows a factor  $\approx 2$  weaker CO and OH lines compared to Peak 1. Most of the water vapor lines are also up to a factor  $\sim 2$  fainter, although some excited H<sub>2</sub>O lines (typically with  $E_u/k > 500$  K) are slightly brighter towards Peak 2. A comparison between the Peak 1 and 2 shortest-wavelength spectra is shown in Figures 2c, 2d and 2e. A closer look to the line profile evolution near 65  $\mu\text{m}$  is shown in Figure 3.

Figure 2 also shows the spectrum toward a position in the ambient cloud (pink histogram) far from the Hot Core and outflows. As an example, the <sup>12</sup>CO  $J=17-16$  line is  $\sim 250$  times weaker than toward Peak 1 and the very high- $J$  CO lines are not even detected. The mid- $J$  <sup>13</sup>CO lines are only marginally detected due to the low sensitivity of SPIRE to detect faint and narrow lines. This shows that much lower column densities of warm CO exist toward the ambient cloud compared to Orion BN/KL (see Peng et al. 2012b, for large-scale <sup>13</sup>CO  $J=8-7$  mapping of OMC1 with APEX). On the other hand, the bright [O III] 88  $\mu\text{m}$  fine structure line from ionized gas shows similar luminosities in both positions, confirming that this is a different structure in the line-of-sight (the foreground ionized nebula illuminated by the Trapezium cluster).

#### 4. ANALYSIS

##### 4.1. Maps of line surface brightness ratios

In addition to the absolute line surface brightness, our multi-line spectral maps allow one to study the spatial variations of different line intensity ratios, all observed with similar angular resolution and calibration accuracy. Figures 4 and 5 show a selection of such maps.

When compared to the [O I] 145  $\mu\text{m}$  optically thin line for example, the CO  $J=21-20$  and the  $J=34-33$  intensity ratio maps suggest the presence of two different physical components, a lower excitation component showing a roughly spherical distribution, and a more excited component that shows a maximum toward the Peak 1 region (Fig. 4c). In particular, the emission of the CO lines with  $J$  from  $\sim 20$  to 25 peak  $\sim 10''$  NE of the Hot Core and shows a low CO  $J=21-20$ /[O I] 145  $\mu\text{m}$  intensity ratio. This may indicate a shocked region where CO is being dissociated. On the other hand, the CO  $J=34-33$ /[O I] 145  $\mu\text{m}$  intensity ratio map peaks toward Peak 1, the same region where the very excited CO lines ( $J > 30$ ) have their intensity peak. The OH/*o*-H<sub>2</sub>O (84.6/75.4  $\mu\text{m}$ ) intensity ratio map (similar Einstein coefficients and upper level energies) shown in Fig. 4a sug-

gests that the OH/H<sub>2</sub>O abundance increases at the outer edge of the outflow(s). Note that, as a consequence of H<sub>2</sub>O photodissociation, the OH/H<sub>2</sub>O intensity ratio gets even higher toward the southernmost regions of the map directly illuminated by the strong UV radiation from the Trapezium cluster (see Goicoechea et al. 2011, for OH observations toward the Orion Bar PDR). Figure 4d shows the *o*-H<sub>2</sub>O 3<sub>21</sub>-2<sub>12</sub>/CO  $J=21-20$  line ratio map. This ratio traces warm gas regions where the water emission is enhanced. The map shows the smallest H<sub>2</sub>O/CO intensity ratios along the NE-SW direction of the quiescent extended ridge and the highest values in the perpendicular direction (the high-velocity outflow).

As a more quantitative (but still approximated) way of investigating the temperature and density gradients in the region, we selected three appropriate CO, H<sub>2</sub>O and OH line intensity ratios and used a non-LTE, LVG radiative transfer code (Cernicharo 2012) to explore their variation over a large parameter space. The assumed column densities follow the observed far-IR line luminosity ratios  $L(\text{CO})/L(\text{H}_2\text{O})/L(\text{OH}) \simeq 5/2/1$  and we chose  $N(\text{OH}) = 10^{16} \text{ cm}^{-2}$  (see Table 2). A line-width of 30  $\text{km s}^{-1}$  representative of Orion outflow(s) was used. The latest available collisional rates were used (Daniel et al. 2011 and references therein for H<sub>2</sub>O, Yang et al. 2010, extended by Neufeld 2012, for CO and van Offer et al 1994 for OH). We used an H<sub>2</sub> *ortho-to-para* (OTP) ratio of 3, the inferred value from H<sub>2</sub> observations in the region (Rosenthal et al. 2000).

Figure 5 shows the spatial distribution of the CO  $J=34-33/21-20$  (77.1/124.2  $\mu\text{m}$ ), *o*-H<sub>2</sub>O 3<sub>21</sub>-2<sub>12</sub>/2<sub>12</sub>-1<sub>01</sub> (75.4/179.5  $\mu\text{m}$ ) and OH <sup>2</sup> $\Pi_{3/2}$   $J=7/2-5/2/5/2-3/2$  (84.6/119.4  $\mu\text{m}$ ) intensity ratios respectively. The grid of non-LTE models of the same line ratio is shown in the *right* column. Note that for a given species the color scale in the intensity ratio map and in the grid of models are the same.

As a first order, the CO  $J=34-33/21-20$  intensity ratio traces (warm gas) temperature variations in the region. Figure 5a shows that the intensity ratio increases with distance to the Hot Core, reaching a maximum value in the NW direction near Peak 1 where the high-velocity outflow plunges into the ambient cloud. These shocked gas regions are characterised by high temperatures (at least  $T_k > 800$  K). Note that a much lower CO 34-33/21-20 ratio is inferred toward the inner Hot Core regions. However, owing to the presumably high far-IR dust opacities toward the Hot Core (see Sect. 4.3), it is difficult to conclude whether the elevated dust opacity attenuates the high- $J$  CO line emission at the shortest far-IR wavelengths or this is just the absence of hot shocked gas toward the Hot Core. The lack of high-velocity CO bullets in the Hot Core region, however, seems to support this latter scenario (see the interferometric observations by Zapata et al. 2009, 2011).

The selected H<sub>2</sub>O and OH line ratios are more sensitive to density variations in the shocked gas. Both Figs. 5a and 5b suggest that the gas density increases toward Peak 1 and 2. In these positions the gas seems compressed by a factor  $\gtrsim 10$ , reaching  $n(\text{H}_2) \approx 10^7 \text{ cm}^{-3}$ . Still, note that the  $T_k$  and  $n(\text{H}_2)$  values suggested in Figure 5 are merely indicative and only show global trends

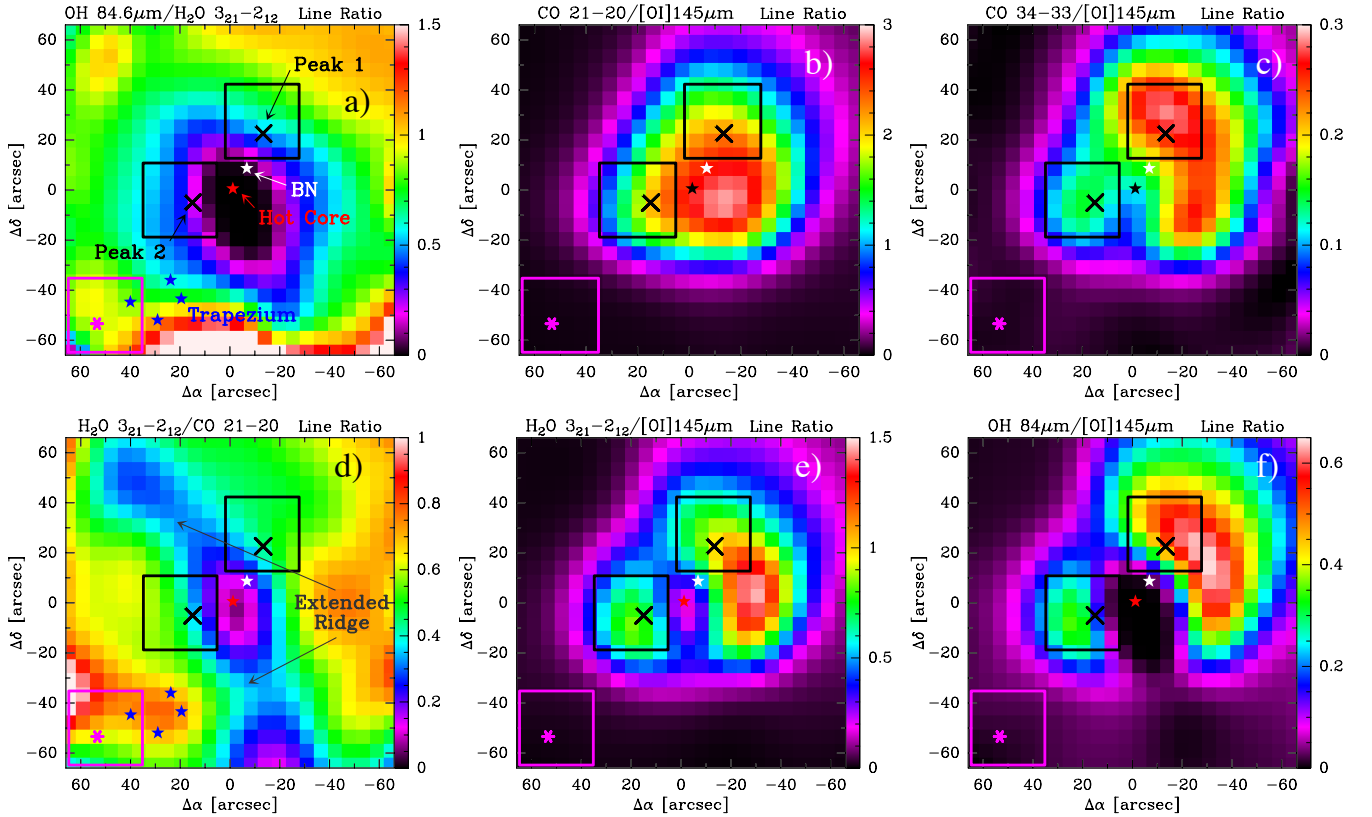


**Figure 4.** Line surface brightness ratios for selected lines observed with *Herschel*/PACS toward Orion BN/KL. The areas used to compute the line luminosities in the three representative regions discussed in the text (Peak 1, Peak 2 and ambient cloud) are shown with black and pink squares respectively. The black crosses and the pink star show the exact positions where the spectra shown in Figure 2 are extracted. The position of the main sources discussed in the text: the Trapezium cluster stars (blue stars), the BN source and the position of the Hot Core (colored stars) are also shown.

in the region. The exact values will depend on the actual column density of material toward each line-of-sight, the local excitation conditions and radiative transfer effects.

Finally, the line ratio maps shown in Figures 4a, 4d and 5 suggest that there are not major differences between the physical conditions prevailing in the Peak 1 region and those of Peak 2 (see also sec. 4.2). In the following, we focus our analysis in the interpretation of the spectra toward Peak 1.

#### 4.2. CO, H<sub>2</sub>O and OH rotational diagrams

Figure 6 shows all CO, H<sub>2</sub>O and OH detected lines toward Peak 1 in a *rotational diagram*. In these plots we assumed extended emission over a  $\sim 30'' \times 30''$  aperture. Owing to the high densities previously inferred toward Peak 1,  $\gtrsim 10^6 \text{ cm}^{-3}$  from H<sub>2</sub> line observations (Rosenthal et al. 2000) and  $\gtrsim 10^7 \text{ cm}^{-3}$  from CO and H<sub>2</sub>O ro-vibrational lines (González-Alfonso et al. 2002), the rotational temperatures ( $T_{\text{rot}}$ ) derived from the CO rotational diagrams are a good lower limit to the gas temperature ( $T_k \gtrsim T_{\text{rot}}$ ).

The <sup>12</sup>CO rotational diagram shows a notable contribution of very high- $J$  lines ( $J > 40$ ) that cannot be fitted with a single rotational temperature in LTE (a straight line in the plot). A similar population diagram of the mid-IR H<sub>2</sub> lines also shows a remarkable positive curvature (Rosenthal et al. 2000). Mid-IR H<sub>2</sub> rotational lines in the ground-vibrational state (up to  $E_u/k \lesssim 10^4 \text{ K}$ ) have low critical densities, of the order of  $10^{2-6} \text{ cm}^{-3}$ , and thus the

curved H<sub>2</sub> level distribution is not compatible with a low-density isothermal component (see also Sect. 6.2). As H<sub>2</sub>, the <sup>12</sup>CO rotational diagram suggests the presence of at least two temperatures components, a warm component with  $T_{\text{rot}} \approx 400 \text{ K}$  and a hotter component with  $T_{\text{rot}} \approx 1000 \text{ K}$ . For comparison, the CO emission in the ambient cloud is dominated by a cooler component with  $T_{\text{rot}} \approx 180 \text{ K}$  (blue triangles in Fig. 6a). This is the warm and extended face-on PDR (the interface between the foreground H II region and the molecular cloud), heated by FUV photons from the Trapezium stars (see Peng et al. 2012b, for large-scale mapping of several mid- $J$  CO narrow lines).

A rotational diagram of the <sup>13</sup>CO lines detected with PACS toward Peak 1 provides  $T_{\text{rot}} \approx 200 \text{ K}$ , thus lower than the  $T_{\text{rot}}$  inferred from <sup>12</sup>CO. The measured <sup>12</sup>CO/<sup>13</sup>CO intensity ratio for the  $J=16-15$  and  $15-14$  lines is  $55 \pm 5$ , lower than the <sup>12</sup>C/<sup>13</sup>C isotopic ratio of  $\sim 79 \pm 7$  in Orion (Langer & Penzias 1990). For  $J > 16$ , however, the <sup>12</sup>CO/<sup>13</sup>CO intensity ratio becomes equal or larger than the isotopic value, showing that while the submm <sup>12</sup>CO low- and mid- $J$  lines are optically thick, the high- $J$  far-IR lines ( $J > 16$ ) are unambiguously optically thin.

H<sub>2</sub>O and OH have a more complex rotational spectroscopy and much higher critical densities than H<sub>2</sub> and CO lines. Therefore, the rotational temperatures inferred from their rotational population diagrams do not



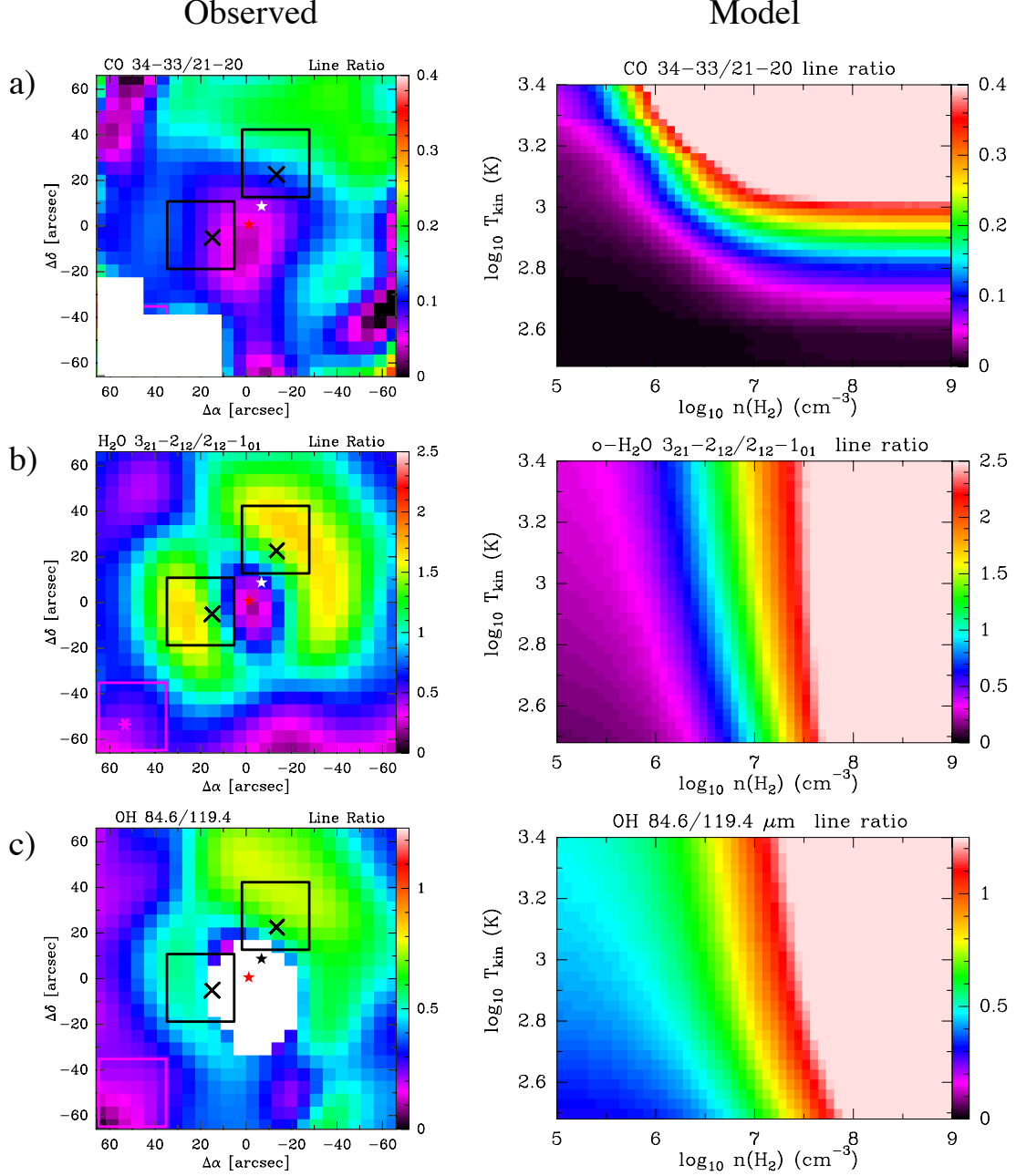


**Figure 5.** Line surface brightness ratios for selected lines observed with *Herschel*/PACS (*left* column) and non-LTE excitation models for the same line intensity ratio (*right* column). The areas used to compute the line luminosities in the three representative regions discussed in the text (Peak 1, Peak 2 and ambient cloud) are shown with black and pink squares respectively. The black crosses and the pink star show the exact positions where the spectra shown in Figure 2 are extracted. The position of the BN source and the position of the Hot Core are also shown in each panel (colored stars). Panels a), b) and c) show the CO  $J=34-33/21-20$  (77.1/124.2  $\mu\text{m}$ ),  $o\text{-H}_2\text{O}$   $3_{21}-2_{12}/2_{12}-1_{01}$  (75.4/179.5  $\mu\text{m}$ ) and OH  $^2\Pi_{3/2}$   $J=7/2-5/2$  /  $5/2-3/2$  (84.6/119.4  $\mu\text{m}$ ) intensity ratios respectively. Note that for a given species, the color scale in the line ratio map and in the grid of models are the same. The blanked pixels (in white) represent either very low S/N emission (for CO) or line absorption detections (for OH).

represent  $T_k$  properly. We show them in Fig. 6b and 6c so that they can be compared with similar diagrams published in the literature (e.g., Karska et al. 2014, and references therein). H<sub>2</sub>O and OH rotational levels are sub-thermally populated ( $T_{\text{rot}} < T_k$ ) and in regions of strong far-IR continuum fields like the Orion Hot Core, they are affected by radiative pumping ( $T_{\text{rot}} < T_d$ ; see e.g., Goicoechea et al. 2006; Cernicharo et al. 2006).

#### 4.3. Simple non-LTE model of Peak 1

In order to constrain the average physical conditions and abundances in the different temperature components suggested by the CO, H<sub>2</sub>O and OH rotational diagrams, we have carried out a simple non-LTE model of the observed emission toward Peak 1.

Our model includes radiative pumping by far-IR dust continuum photons. In particular, we add the effects of a modified black body source with a radius of 10'' and a

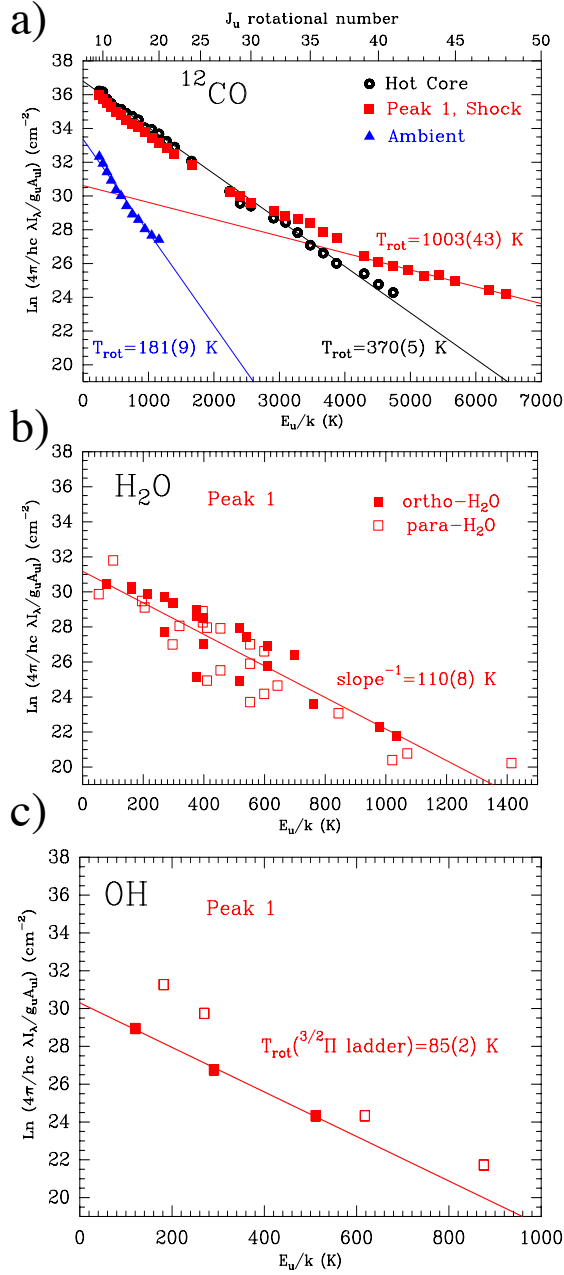


**Figure 6.** Rotational population diagrams obtained from *Herschel*/PACS and SPIRE observations of the Peak 1 region in a  $\sim 30'' \times 30''$  aperture. *a*)  $^{12}\text{CO}$  rotational diagram also showing the corresponding data toward the ambient cloud (shown in Figure 1 with a pink square) and toward the Hot Core, all in apertures of the same size. The straight lines and associated rotational temperatures show fits to the data set in different  $J$  ranges. *b*)  $o$ - and  $p$ - $\text{H}_2\text{O}$  rotational diagram. A single straight line is fitted to all points. *c*) OH rotational diagram.  $T_{\text{rot}}$  is calculated by fitting OH lines in the  $^2\Pi_{3/2}$  rotational ladder only.

dust color temperature of 100 K. The continuum source is optically thick at  $100\ \mu\text{m}$  (with  $\tau_\lambda = 7 [100/\lambda(\mu\text{m})]^2$ ). These values were obtained by fitting the far-IR PACS continuum and the mid-IR photometric observations obtained by *SOFIA*/FORECAST in a  $\sim 30'' \times 30''$  aperture around the Hot Core and IRC sources (De Buizer et al. 2012). The modelled gas components were placed at  $25''$  from the continuum source.

We follow previous studies of the CO and  $\text{H}_2\text{O}$  rotational and ro-vibrational emission observed with *ISO*. In particular, a detailed excitation analysis of the CO  $v=1-0$  and  $\text{H}_2\text{O}$   $v_2=1-0$  bands (observed with the  $14'' \times 20''$  aperture of *ISO*/SWS; González-Alfonso et al. 2002) concluded that the CO vibrational band at  $\sim 4.7\ \mu\text{m}$  can be reproduced with two dense ( $n(\text{H}_2) \sim 2 \times 10^7\ \text{cm}^{-3}$ ) temperature components of shock-excited material; a *warm* one with  $T_k \sim 200\text{--}400\ \text{K}$  and a *hot* component with  $T_k \sim 3000\ \text{K}$ . This high density is in principle consistent with the compression factors suggested by our intensity ratio maps (Fig. 5b and 5c) and with the presence of excited emission lines from high density tracers like HCN.

In our model, the *hot* and *warm* components have a size of  $10''$ , consistent with the compact spatial distribution of the very high- $J$  CO lines toward Peak 1 (see Fig. 1g and Sempere et al. 2000). Figure 8 shows the observed CO line fluxes as a function of  $J$ . The distribution of line fluxes shows a maximum at  $J=17$  and an emission tail at  $J>40$ . The CO lines with  $J<20$  show a more extended spatial distribution than the higher- $J$  lines (Fig. 1i) suggesting that a third, *cool* and extended component needs to be included to fit the CO lines below  $J=20$ . We adopt a line-width of  $30\ \text{km s}^{-1}$  in all modelled components. This is consistent with the wide-angle high-velocity outflow and with the typical line-widths of CO,  $\text{H}_2\text{O}$  and many other species observed at heterodyne spectral resolution in the plateau (e.g., Blake et al. 1987; Melnick et al. 2010; Tercero et al. 2010).

#### 4.3.1. $^{12}\text{CO}$ and $^{13}\text{CO}$ model

The presence of *hot* gas with  $T_k > 1000\ \text{K}$  was first inferred from  $\text{H}_2$  ro-vibrational temperatures (Beckwith et al. 1978; Rosenthal et al. 2000) and is also needed to fit the high energy CO  $v=1-0$  ro-vibrational emission (González-Alfonso et al. 2002). In the far-IR spectrum, this component becomes apparent in the CO  $J>40$  ( $E_u/k > 4513\ \text{K}$ ) emission tail. Figure 7 shows synthetic  $^{12}\text{CO}$  rotational temperatures in the  $J=41\text{--}48$  range obtained from a grid of single-temperature non-LTE models. It shows that for densities in the range  $n(\text{H}_2) \sim 10^{6.2}$  to  $10^8\ \text{cm}^{-3}$ , the gas temperatures required to produce

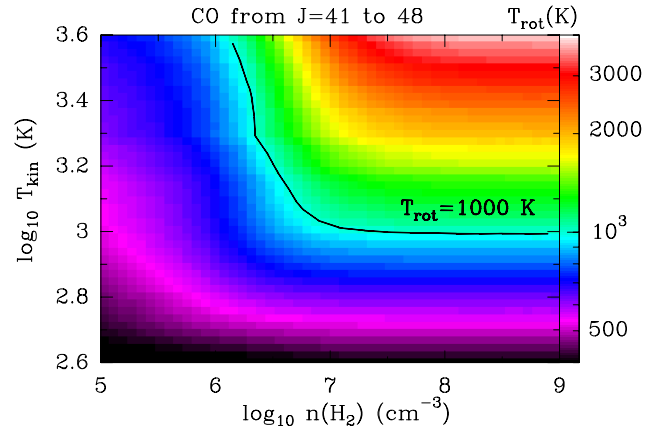


**Figure 7.** Synthetic  $^{12}\text{CO}$  rotational temperatures ( $J=41\text{--}48$  range) obtained from a grid of single-temperature non-LTE models with  $N(\text{CO}) = 5 \times 10^{16}\ \text{cm}^{-2}$ . The  $T_{\text{rot}} = 1000\ \text{K}$  isocontour is shown as a black curve. This is the  $T_{\text{rot}}$  inferred from the very high- $J$  CO lines observed with PACS toward Peak 1.

**Table 1**

Model components and resulting source-averaged column densities toward Peak 1 (assuming a line-width of 30 km s<sup>-1</sup>).  
<sup>†</sup>Assuming no contribution in the *hot* component (see text).

Component	$T_k$ (K)	$n(\text{H}_2)$ (cm <sup>-3</sup> )	Size (arcsec)	$N(\text{CO})$ (cm <sup>-2</sup> )	$N(\text{H}_2\text{O})$ (cm <sup>-2</sup> )	$N(\text{OH})$ (cm <sup>-2</sup> )
<i>Hot</i> shock-excited	~2500	~2×10 <sup>7</sup>	~10	~1.5×10 <sup>16</sup>	~2.0×10 <sup>16</sup>	~1.5×10 <sup>16</sup>
<i>Warm</i> shock-excited	~500	~2×10 <sup>7</sup>	~10	~2.0×10 <sup>19</sup>	(~2.0×10 <sup>17</sup> ) <sup>†</sup>	(~5.0×10 <sup>16</sup> ) <sup>†</sup>
<i>Cool</i> plateau outflow(s)	~200	~2×10 <sup>6</sup>	~30	~2.0×10 <sup>19</sup>	~6.7×10 <sup>17</sup>	~1.5×10 <sup>17</sup>

$T_{\text{rot}}(\text{CO}) \simeq 1000$  K for  $J > 40$  are very high, in the range  $T_k \simeq 3500$  to 1000 K respectively.

The *warm* and *hot* components dominate the CO line emission for  $J > 20$ . Assuming the same H<sub>2</sub> densities inferred from the CO  $v=1-0$  band analysis, we run models varying  $T_k$  and  $N(\text{CO})$  around the values derived by González-Alfonso et al. (2002) and Sempere et al. (2000). A good fit to the data is found for  $T_{k,\text{warm}} \simeq 500$  K and  $T_{k,\text{hot}} \simeq 2500$  K. The inferred source-averaged CO column densities are similar to those inferred from the CO  $v=1-0$  vibrational band:  $N(\text{CO})_{\text{warm}} \simeq 2.0 \times 10^{19}$  cm<sup>-2</sup> and  $N(\text{CO})_{\text{hot}} \simeq 1.5 \times 10^{16}$  cm<sup>-2</sup>.

A third *cooler* and more extended component is needed to reproduce the <sup>12</sup>CO and <sup>13</sup>CO emission with  $J < 20$ . We associate this component with the extended plateau (outflowing and swept-up material). The gas density in the plateau is estimated to be  $n(\text{H}_2) \approx (1-2) \times 10^6$  cm<sup>-3</sup> (e.g., Blake et al. 1987; Melnick et al. 2010; Tercero

et al. 2010). This is, at least a factor 10 lower than in the shock-excited gas traced by the very high- $J$  CO rotational lines and by the CO  $v=1-0$  band (*hot* and *warm* components). Modelling all components together (adding the emission from each component) we obtain a satisfactory fit to the CO ladder with  $T_{k,\text{plat}} \simeq 200$  K,  $n(\text{H}_2) \simeq 2 \times 10^6$  cm<sup>-3</sup> and  $N(\text{CO})_{\text{plat}} \simeq 2 \times 10^{19}$  cm<sup>-2</sup> for the *cool* component (Fig. 8). The complete model agrees with observations within a ~20 % and is also consistent with the <sup>13</sup>CO lines assuming a <sup>12</sup>C/<sup>13</sup>C isotopic ratio of 80.

#### 4.3.2. H<sub>2</sub>O model

The extended plateau in Orion BN/KL shows enhanced H<sub>2</sub>O column densities compared to more quiescent interstellar environments. Still, the exact water vapor abundances are controversial (*cf.* Cernicharo et al. 1994, 1999, 2006; Harwit et al. 1998; Wright et al. 2000; Melnick et al. 2000, 2010). Most of these observations were carried out toward the core of Orion BN/KL where a very strong mid- and far-IR radiation field from the Hot Core region exists. The angular resolution of the above observations range from the ~3' and ~80'' of SWAS and the ISO/LWS, to the 44''-12'' beam of *Herschel*/HIFI in the submm. The ~12'' resolution of *Herschel*/PACS allows us to resolve the intrinsic H<sub>2</sub>O emission toward Peak 1. In addition, the continuum emission is significantly weaker and lines are not contaminated by absorption toward the Hot Core.

A single temperature component can not fit the observed H<sub>2</sub>O emission lines toward Peak 1. However, most of the H<sub>2</sub>O lines with  $E_k/k < 750$  K can be reasonably fitted with the extended plateau component ( $T_{k,\text{plat}} \simeq 200$  K,  $n(\text{H}_2) \simeq 2 \times 10^6$  cm<sup>-3</sup> and  $N(\text{H}_2\text{O})_{\text{plat}} \simeq 6.7 \times 10^{17}$  cm<sup>-2</sup>). This agrees with detailed models of H<sub>2</sub>O lines detected by *Herschel*/HIFI toward the Hot Core position (Melnick et al. 2010).

Even taking into account the moderate far-IR radiation field toward Peak 1, the H<sub>2</sub>O lines arising from higher energy levels require higher excitation conditions. The detailed excitation analysis of the H<sub>2</sub>O  $v=1-0$  vibrational band at ~6.7 μm toward Peak 1 concluded that hotter and denser gas contributes to the mid-IR H<sub>2</sub>O ro-vibrational emission. Since abundant water vapor is expected in the hot excited-gas, we included H<sub>2</sub>O in the *hot* CO component to match the water emission lines with  $E_k/k > 750$  K. A good fit is obtained for  $N(\text{H}_2\text{O})_{\text{hot}} \simeq 2 \times 10^{16}$  cm<sup>-2</sup>. Figure 9 shows that the lower excitation extended plateau component (blue dots) does not contribute much to the higher energy H<sub>2</sub>O line fluxes. On the other hand, the *hot* water component (red dots) contributes to a small fraction of the low excitation H<sub>2</sub>O line fluxes. In the *hot* component we infer a high H<sub>2</sub>O/CO ≈ 1.3 abundance ratio. Given the simplicity of

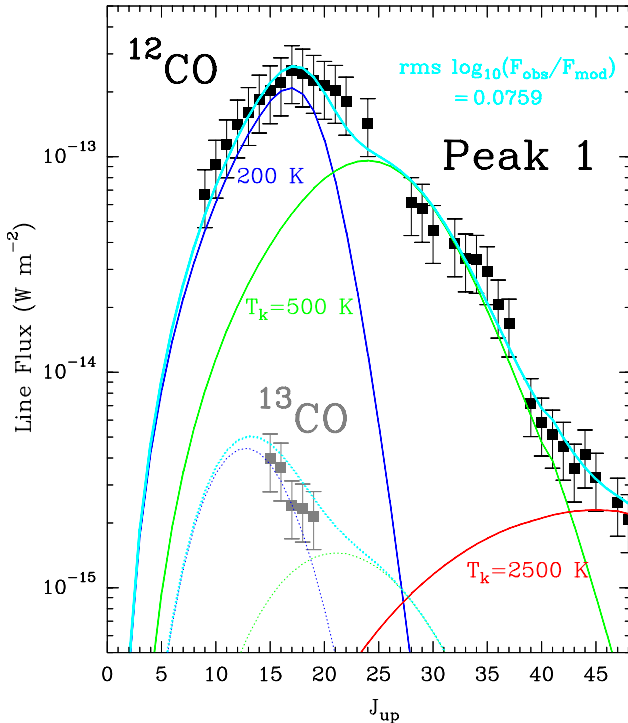


**Figure 8.** <sup>12</sup>CO and <sup>13</sup>CO line fluxes observed by *Herschel*/PACS and SPIRE toward Orion Peak 1 and non-LTE excitation and radiative transfer model results (continuous and dashed curves for <sup>12</sup>CO and <sup>13</sup>CO respectively). The blue curves represent the contribution of the ~200 K (*cool* plateau) component, the green curves represent the ~500 K (*warm* shock-excited) component and the red curve represents the ~2500 K (*hot* shock-excited) component. The cyan curves show the result of adding all modeled temperature components.

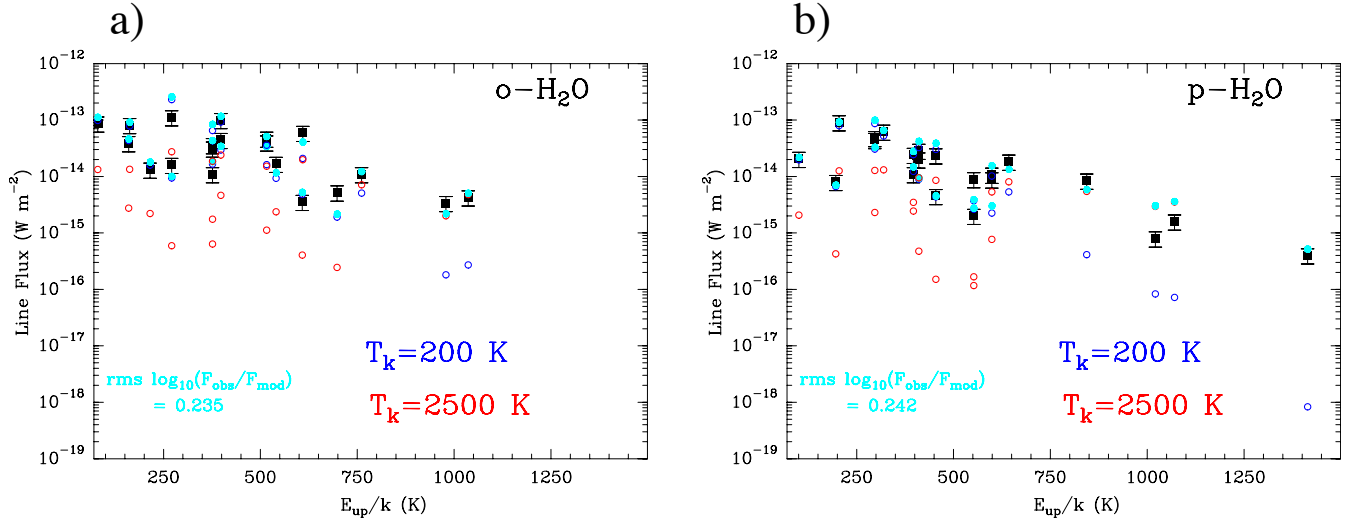


**Figure 9.** *o*-H<sub>2</sub>O and *p*-H<sub>2</sub>O line fluxes observed by *Herschel*/PACS and SPIRE toward Orion Peak 1 and model results. The cyan dots are a model adding the two temperature components (see text).

our model (no radiative coupling between the different components), the global factor  $<2$  agreement is reasonable. The best fit is compatible with an H<sub>2</sub>O OTP ratio of 3. For completeness we also computed the maximum allowable H<sub>2</sub>O column density in the *warm* component ( $T_k \simeq 500$  K) if the high excitation H<sub>2</sub>O lines would not arise from the *hot* component ( $T_k \simeq 2500$  K). We find  $N_{\text{warm}}(\text{H}_2\text{O}) \simeq 2 \times 10^{17} \text{ cm}^{-2}$ , which results in a (modest) maximum  $\text{H}_2\text{O}/\text{CO} \leq 10^{-2}$  abundance ratio. This suggests that high postshock temperatures  $>500$  K are needed to produce high water vapor abundances.

#### 4.3.3. OH model

Previous OH low-angular resolution far-IR observations with *KAO* ( $\sim 33''$ ) and *ISO* ( $\sim 80''$ ) unambiguously showed the presence OH in the outflows expanding from Orion BN/KL (the extended plateau component). This is inferred from the observed line-widths and the P-Cygni profiles (Betz & Boreiko 1989; Melnick et al. 1990; Goicoechea et al. 2006). Our higher angular resolution observations show a pure absorption OH line spectrum toward the Hot Core (Fig. 3) except for the  $\sim 163 \mu\text{m}$  doublet that is mainly excited by far-IR continuum photons. The absorbing regions, with a size of  $\sim 15'' \times 20''$  around the strong continuum peak (see maps in Fig. 1) reduce the OH line emission fluxes when observed at low angular and spectral resolution. Outside the strong far-IR continuum emission regions, all OH lines switch to emission and they peak toward the bright H<sub>2</sub> Peaks 1 and 2.

As H<sub>2</sub>O, a single temperature component can not reproduce the observed OH emission toward Peak 1. Following Goicoechea et al. (2006), we model the lower energy OH transitions in the extended plateau. A satisfactory fit is obtained for  $N(\text{OH})_{\text{plat}} \simeq (1.0\text{--}1.5) \times 10^{17} \text{ cm}^{-2}$  (or a  $N(\text{OH})/N(\text{H}_2\text{O}) \simeq 0.15\text{--}0.22$ ). However, this model underestimate the fluxes of the OH higher energy transitions. Such lines likely arise from more excited gas, simulated here by the *warm* and *hot* components.

We find that if the excited OH emission mainly arises from the *warm* CO component at  $T_{k, \text{warm}} \simeq 500$  K, then a

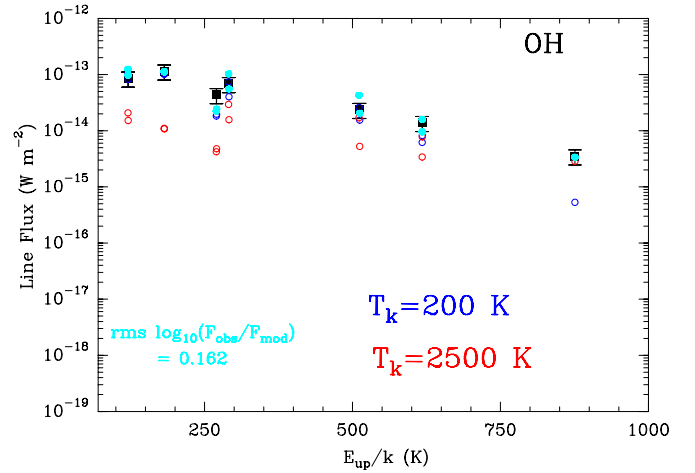


**Figure 10.** OH line fluxes observed by *Herschel*/PACS and SPIRE toward Orion Peak 1 and model results. The cyan dots are a model adding the two temperature components (see text).

$\text{OH}/\text{CO} \simeq 4 \times 10^{-3}$  column ratio satisfactorily reproduces the excited OH lines. On the other hand, if the excited OH lines arise from the *hot* CO component at  $\simeq 2500$  K, then a model with roughly equal amounts of hot CO, H<sub>2</sub>O and OH are needed to fit the excited lines. All in all, the combined extended plateau + *hot* or + *warm* OH model reasonably agrees with observations within a  $\sim 20\%$  (Fig. 10). Taking into account both scenarios, the source-averaged OH column density in the dense shock-excited component is  $N(\text{OH}) \simeq (1.5\text{--}5.0) \times 10^{16} \text{ cm}^{-2}$ .

#### 4.4. Molecular Abundances toward Peak 1

The absolute water vapor abundance with respect to H<sub>2</sub> has long been discussed in many different protostellar environments. The old prediction that copious amounts of H<sub>2</sub>O, and to a lower extent O<sub>2</sub>, will be produced behind molecular shocks has been challenged by several *Herschel* observations (e.g., Goldsmith et al. 2011; van Dishoeck et al. 2013). Unfortunately, even in the  $\sim 10\text{--}40''$  beam of *Herschel*, different physical components usually overlap and it is not obvious to extract their relative

abundances with accuracy (e.g., Chen et al. 2014).

Taking  $N(\text{H}_2) \approx 10^{23} \text{ cm}^{-2}$  in a  $30''$  beam for the *cool* plateau component (Blake et al. 1987; Melnick et al. 2010), we obtain  $\chi_{\text{plat}}(\text{CO}) \approx 2 \times 10^{-4}$ ,  $\chi_{\text{plat}}(\text{H}_2\text{O}) \approx 0.7 \times 10^{-5}$  and  $\chi_{\text{plat}}(\text{OH}) \approx 0.2 \times 10^{-5}$  abundances. Hence, in the less excited swept-up gas, water vapor is not the dominant O-bearing species. However, if we only consider the *hot* shock-excited component, the derived H<sub>2</sub>O/CO abundance ratio is much higher ( $\sim 1.3$ ). Rosenthal et al. (2000) inferred that the column density of hot H<sub>2</sub> with  $T_{\text{ex}} > 1200 \text{ K}$  toward Peak 1 is  $N(\text{H}_2) \lesssim 10^{20} \text{ cm}^{-2}$ . Taking the columns from this component alone, we determine  $\chi_{\text{hot}}(\text{H}_2\text{O}) \gtrsim 2 \times 10^{-4}$ ,  $\chi_{\text{hot}}(\text{CO}) \gtrsim 1.5 \times 10^{-4}$  and  $\chi_{\text{hot}}(\text{OH}) \gtrsim 0.8 \times 10^{-5}$ .

#### 4.5. Model uncertainties and Peak 1/2 differences

Our multi-component model satisfactorily reproduces the fluxes of most observed lines. Despite this model solution is certainly not unique, the agreement with observations suggests that the model captures the average physical conditions of the shocked-exited gas.

The best fit to the CO  $J=41$  to 48 absolute line fluxes alone gives  $T_k \simeq 2300\text{--}3000 \text{ K}$  and  $n(\text{H}_2) \simeq (3\text{--}4) \times 10^6 \text{ cm}^{-3}$  for  $N(\text{CO}) = (5.0\text{--}2.5) \times 10^{16} \text{ cm}^{-2}$  for Orion Peak 1. These values suggest that the postshock gas where the high-excitation CO, H<sub>2</sub>O and OH lines arise might be up to  $\sim 5$  times less dense than our assumed value of  $n(\text{H}_2) \simeq 2 \times 10^7 \text{ cm}^{-3}$  (but see Sempere et al. 2000; González-Alfonso et al. 2002). In such a case, the H<sub>2</sub>O column densities in the *hot* component will be a factor  $\sim 4$  higher and the H<sub>2</sub>O/CO abundance ratio will increase from  $\sim 1.3$  to  $\sim 1.6$ . Finally, the presence of a moderate far-IR dust radiation field helps to better fit the fluxes of several H<sub>2</sub>O and OH lines. Although the radiative pumping effects toward Peak 1 are less dramatic than toward the Hot Core, neglecting the presence of a far-IR field will overestimate the the resulting  $N(\text{OH})$  and  $N(\text{H}_2\text{O})$  by  $\sim 50\%$ . These numbers should be considered as the range of uncertainty in the physical conditions from our simple model (up to a factor  $\sim 5$  in the absolute volume and column densities).

Our data show small differences between Peak 1 and 2. The CO and OH rotational temperatures we infer toward Peak 2 are similar to those toward Peak 1 (despite lines are up to a factor  $\sim 2$  brighter). Only some excited H<sub>2</sub>O lines are slightly stronger toward Peak 2 (producing higher H<sub>2</sub>O rotational temperatures by  $\lesssim 20\%$ ) and suggesting that the water vapor column and probably the gas density are also slightly higher. Note that the same conclusions were reached from the observation of the CO and H<sub>2</sub>O vibrational bands (González-Alfonso et al. 2002). However, we estimate that the aperture-averaged column densities and the physical conditions differences between both peaks are within a factor  $\sim 2$  (see also Figure 10). Therefore, they are smaller than the range of uncertainties in our models and thus we have not modeled both peaks independently.

#### 5. GAS COOLING IN ORION H<sub>2</sub> PEAK 1 SHOCK

Table 2 summarizes the observed line and continuum luminosities in a  $\sim 30'' \times 30''$  aperture toward the H<sub>2</sub> Peak 1 position. They provide a good measurement of

**Table 2**  
Observed luminosities and cooling budget (assuming  $d=414 \text{ pc}$ )

Species	$L_{\text{obs}} (L_{\odot})$ in Peak 1 <sup>c</sup>	% <sup>a</sup> in Peak 1 <sup>c</sup>	$L_{\text{obs}} (L_{\odot})$ in map <sup>c</sup>	% <sup>b</sup> in map <sup>c</sup>
FIR <sup>12</sup> CO	18.7	$\sim (22 \pm 5)\%$	84	$\sim 31\%$
FIR H <sub>2</sub> O	7.0	$\sim (8 \pm 2)\%$	32	$\sim 12\%$
FIR OH	3.5	$\sim (4 \pm 1)\%$	13	$\sim 5\%$
FIR [O I]	3.5	$\sim (4 \pm 1)\%$	18	$\sim 7\%$
FIR [C II]	0.3	$\sim (0 \pm 0)\%$	7	$\sim 3\%$
FIR <sup>13</sup> CO	0.3	$\sim (0 \pm 0)\%$	2	$\sim 1\%$
<sup>12</sup> CO $v=1\text{--}0$	$\sim 6.1^d$	$\sim 7\%$	$\sim 14^d$	$\sim 5\%$
H <sub>2</sub> O $v_2=1\text{--}0$	$\sim 1.3^d$	$\sim 2\%$	$\sim 3^d$	$\sim 1\%$
MIR H <sub>2</sub>	$\sim 43^e$	$\sim 51\%$	$\sim 102^e$	$\sim 37\%$
Total	$\sim 84$	100%	274	100%
FIR dust	$\sim 4 \times 10^3$	-	$\sim 10^5$	-

<sup>a</sup> In a  $\sim 30'' \times 30''$  aperture ( $\sim 12500 \text{ AU} \times 12500 \text{ AU}$ ).

<sup>b</sup> In the entire  $\sim 2' \times 2'$  map ( $\sim 0.25 \text{ pc} \times 0.25 \text{ pc}$ ).

<sup>c</sup> Absolute calibration accuracy up to  $\pm 30\%$ .

<sup>d</sup> Scaled from ISO/SWS observations (González-Alfonso et al. 2002).

<sup>e</sup> Scaled from ISO/SWS observations (Rosenthal et al. 2000).

the cooling budget in shocked gas. This tabulation also includes an extrapolation of the mid-IR H<sub>2</sub> line fluxes and of the CO and H<sub>2</sub>O ro-vibrational emission detected by ISO/SWS (Rosenthal et al. 2000; González-Alfonso et al. 2002). Their measured luminosities have been multiplied by  $(30'' \times 30'') / (14'' \times 20'') \simeq 3$  to approximately take into account the different aperture sizes. Roughly half of the total line luminosity is provided by H<sub>2</sub> rotational and vibrational line cooling. CO is the next most important species, providing  $\sim (22 \pm 7)\%$  of the total line luminosity (far + mid-IR). H<sub>2</sub>O only contributes with  $\sim (8 \pm 2)\%$  and this may sound surprising in light of previous shock model expectations for Orion (e.g., Draine & Roberge 1982; Kaufman & Neufeld 1996). [O I] and OH lines contribute to line cooling in similar amounts: with  $L(\text{O I})/L(\text{H}_2\text{O}) \simeq 0.4$  and  $L(\text{OH})/L(\text{H}_2\text{O}) \simeq 0.5$ . Taking into account the far-IR range alone, CO rotational lines clearly dominate the gas cooling toward Peak 1 with a very high  $L_{\text{FIR}}(\text{CO})/\text{FIR}$  luminosity ratio of  $\approx 5 \times 10^{-3}$ . Note that the typical luminosity ratio in bright PDRs is below a few  $10^{-4}$  (the value in the Orion Bar, Joblin et al. 2015). In addition, the estimated dust temperatures in the region ( $T_d \approx 100 \text{ K}$ ) are significantly lower than the inferred gas temperatures. Hence, grain-gas collisions can also contribute to the gas cooling.

Assuming that our simple model provides a good representation of the average conditions toward Peak 1, we can also discuss the relative contribution of H<sub>2</sub>O, CO and OH cooling in the different temperature components. In our model we find that CO in the *hot* component ( $T_k \simeq 2500 \text{ K}$ ) only contributes  $\sim 1\text{--}2\%$  to the total CO rotational emission. Indeed, the CO column density in the *hot* component is  $\sim 10^3$  times smaller than in the *warm* component ( $T_k \simeq 500 \text{ K}$ ). On the other hand, the H<sub>2</sub>O emission from the *hot* component contributes with  $\sim 40\%$  of the total H<sub>2</sub>O rotational emission. In particular we predict a H<sub>2</sub>O/CO  $\simeq 1.3$  abundance ratio and a H<sub>2</sub>O/CO  $\simeq 10$  luminosity ratio in the *hot* component alone. Although these numbers are not exact and depend on the model assumptions, they suggest that *it is*



only in the hot ( $>500$  K) postshock gas where water vapor lines dominate the cooling over CO lines.

Considering the rotational line cooling in both the hot and warm components together, the modelled  $\text{H}_2\text{O}/\text{CO}$  luminosity ratio is  $\simeq 0.3$ . For comparison, a  $\text{H}_2\text{O}/\text{CO} \simeq 0.2$  ratio was inferred from the  $\text{H}_2\text{O}$  and CO vibrational bands (González-Alfonso et al. 2002). This means that *considering all components in the shock-excited gas toward Peak 1 together, CO, and not water vapor, is the most important gas coolant after  $\text{H}_2$ .*

## 6. SHOCK(S) PROPERTIES

Fast dissociative shocks can destroy molecules and ionize atoms, whereas slower shocks heat the gas to high temperatures without destroying molecules (e.g., Le Bourlot et al. 2002, for Orion-KL). Depending on the shock wave velocity ( $v_s$ ), pre-shock gas density and magnetic field strength and orientation it is common to distinguish between *J*-type (*Jump*) and *C*-type (*Continuous*) shocks. More complicated, “mixed” non-stationary situations (*CJ*-type) may also exist (Draine & McKee 1993; Walmsley et al. 2005; Lesaffre et al. 2004; Flower & Pineau des Forêts 2013).

Early steady-state planar shock models interpreted the available observations of Orion outflows in the frame of a non dissociative *C*-type shock with preshock densities of several  $10^5 \text{ cm}^{-3}$ ,  $v_s \simeq 36\text{--}38 \text{ km s}^{-1}$  and a magnetic field perpendicular to the shock propagation close to 1 mG (see e.g., Draine & Roberge 1982; Chernoff et al. 1982). At these high shock velocities, vaporization of ice grain mantles is expected (Draine et al. 1983). In addition the gas reaches elevated postshock temperatures (well above  $\sim 1000$  K). Both effects lead to a drastic enhancement of the water vapor abundance. These parameters of a single shock, however, should be taken as an average of the different shock-excited regions included in the large  $\sim 1'$  beam of the early near- and far-IR observations (Genzel & Stutzki 1989). Using a more detailed description of the gas-phase chemistry, molecular cooling and ion-neutral coupling, new *C*-shock models confirmed those shock parameters and predicted that large abundances of  $\text{H}_2\text{O}$ , above  $10^{-4}$  with respect to  $\text{H}_2$ , will form in the postshock gas (all the oxygen not incorporated in CO; Kaufman & Neufeld 1996; Bergin et al. 1998). Alternative models try to explain the  $\text{H}_2$  rotational and vibrational line emission toward Peak 1 (Rosenthal et al. 2000) with a two-component *C*-shock with lower preshock density ( $\sim 10^4 \text{ cm}^{-3}$ ) and two shock wave velocities,  $v_s = 60$  and  $40 \text{ km s}^{-1}$  (Le Bourlot et al. 2002). For the expected shock parameters in Orion, all these models predict that the  $\text{H}_2\text{O}$  line emission will be the second more important gas coolant agent after  $\text{H}_2$ . They also predict high  $\text{H}_2\text{O}/\text{CO}$  abundance ratios  $>1$  in the postshock gas. Our observations, however, show that  $\text{H}_2\text{O}$  lines (rotational and ro-vibrational) are only responsible of  $\sim 10\%$  of the total luminosity emitted by  $\text{H}_2$ , CO,  $\text{H}_2\text{O}$  and O. In addition, the observed far-IR  $L(\text{H}_2\text{O})/L(\text{CO})$  luminosity ratio toward Peak 1 is  $\simeq 0.4$ , at least an order of magnitude lower than the best *C*-shock model predictions for Orion. Perhaps the most intriguing discrepancy is the high observed far-IR  $L(\text{OH})/L(\text{H}_2\text{O}) \simeq 0.5$  luminosity ratio, either suggesting that water vapor formation is not so efficient or that an additional  $\text{H}_2\text{O}$  destruction mechanism (enhancing OH) exists.

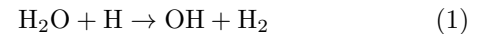
### 6.1. Low $\text{H}_2\text{O}$ abundances: O depletion? Dissociation?

Most early shock models in the literature assumed high initial abundances of either  $\text{O}_2$  molecules or O atoms in the preshocked gas. Hence, for moderate shock velocities  $\gtrsim 10\text{--}15 \text{ km s}^{-1}$  (raising the postshock gas temperature to  $T_k \gtrsim 400$  K) most of the available oxygen was converted into high abundances of water vapor through efficient gas-phase neutral-neutral reactions (e.g., Bergin et al. 1998, and references therein). However, *ISO*, *SWAS*, *ODIN*, and most recently *Herschel* observations suggest that there is far less  $\text{H}_2\text{O}$  (Bergin & Snell 2002; Klotz et al. 2008; Caselli et al. 2010; 2012) and  $\text{O}_2$  (Goldsmith et al. 2000; Pagani et al. 2003; Goldsmith et al. 2011) in quiescent dark clouds than would be expected if atomic oxygen were very abundant. In fact, a wealth of observations unambiguously show that most of the water in cold dark clouds is locked as ice mantles (see van Dishoeck et al. 2013, for review).

Dark cloud observations also suggest that *an undetermined fraction of O atoms stick to grains, thus limiting the oxygen reservoir for water vapor formation*. Indeed, recent investigations do show that atomic oxygen is being depleted even from diffuse clouds at a rate that cannot be accounted for its presence in oxygen-rich dust grains (Jenkins 2009). This implies that a unidentified reservoir of depleted oxygen is already present before the onset of freeze-out in cold dark clouds (before star-formation begins) thus reducing the availability of O atoms (see also Whittet 2010). Unfortunately, the adsorption energy of O atoms to ice is not fully constrained (Hasegawa & Herbst 1993; Hollenbach et al. 2009). Adsorption energies higher than the usually assumed value of  $\sim 800$  K (similar to CO) would imply significant O atom depletion in molecular clouds (see Melnick et al. 2012).

With fewer O atoms in the gas-phase than previously assumed and most of the  $\text{H}_2\text{O}$  locked as ice mantles, fast shocks ( $\gtrsim 25 \text{ km s}^{-1}$ ) are necessarily needed to sputter the frozen-out  $\text{H}_2\text{O}$  (Draine 1995) and produce high abundances of water vapor. Therefore, *only fast shocks characterized by high postshock gas temperatures ( $>1000$  K) will show high gas-phase  $\text{H}_2\text{O}/\text{CO} \gtrsim 1$  abundance ratios* (see also Neufeld et al. 2014). Slower shocks, however, heat the gas to a few hundred K but do not sputter the ice mantles. *Combined with a reduced initial abundance of gas-phase O atoms, slow shocks will produce regions with lower  $\text{H}_2\text{O}/\text{CO}$  abundance ratios ( $\ll 1$ ).*

In the presence of strong UV radiation fields (see also Sect. 6.3), water vapor is photodissociated and leads to high  $\text{OH}/\text{H}_2\text{O} \gtrsim 1$  abundance ratios (see Goicoechea et al. 2011, for the Orion Bar PDR). In addition, the endothermic reaction (a few thousand K):



can convert some  $\text{H}_2\text{O}$  into OH if the gas is hot enough, and if free H atoms are available (if a fraction of  $\text{H}_2$  molecules are dissociated). These are conditions characteristic of, at least partially dissociative, *J*-shocks (Neufeld & Dalgarno 1989; Hollenbach & McKee 1989). H I observations show that a fraction of H atoms do exit in Orion’s outflows. In particular, the H I emission in the  $v_{\text{LSR}} = 19$  to  $31 \text{ km s}^{-1}$  range follows the orientation of the high-velocity outflow (van der Werf et al. 2013). Hence, it is plausible that *J*-shock spots with a non neg-



ligible H<sub>2</sub> dissociation fraction exist.

A firmer evidence may come from the observed line surface brightness of species like OH or O. Their emission lines are predicted to be weak in non-dissociative *C*-shocks and bright in dissociative *J*-shocks. As an example, the OH ground-state line at  $\sim 119.4\mu\text{m}$  and the [O I]  $63\mu\text{m}$  line toward Peak 1 are very bright,  $\sim 4 \times 10^{-6} \text{ W m}^{-2} \text{ sr}^{-1}$  and  $\sim 3 \times 10^{-5} \text{ W m}^{-2} \text{ sr}^{-1}$  respectively. In the recent shock models of Flower & Pineau des Forêts (2013), these intensities can only be reproduced by relatively dense preshock gas ( $> 10^5 \text{ cm}^{-3}$ ) subjected to *J*-type shocks. In this context, the decrease of the observed H<sub>2</sub>O  $3_{21-2_{12}}$ /[O I]  $145\mu\text{m}$  line intensity ratio (and increase of the OH  $84.6\mu\text{m}$ /[O I]  $145\mu\text{m}$  ratio) toward Peak 1 (Figures 4e and 4f) are consistent with H<sub>2</sub>O dissociation in the shock.

### 6.2. Mixed *C*- and *J*-type shocks

The strong H<sub>2</sub> line luminosities toward Peak 1 and their implied excitation temperatures (up to  $\sim 3000 \text{ K}$  Rosenthal et al. 2000) are not entirely compatible with dissociative *J*-shocks in which molecules are destroyed by collisional dissociation. Although the atomic gas is initially very hot (and UV radiation), by the time that molecules reform the gas has cooled to about  $500 \text{ K}$  (e.g., Neufeld & Dalgarno 1989; Hollenbach & McKee 1989). Therefore, *J*-type shocks are a plausible source of UV radiation in downstream molecular gas and may contribute to the *warm* CO component ( $T_k \sim 500 \text{ K}$ ) and that shows emission peaks both toward Peak 1 and also  $\sim 10''$  NE of the Hot Core). These positions likely represent the apex of the high-velocity and low-velocity outflows interacting with the ambient cloud. Indeed,  $\sim 10''$  resolution observations of the [C I]  $3P_2-3P_1$  and CO  $J=7-6$  lines with the CSO suggest a  $\sim 20''$  shell structure of atomic carbon at the edge of the region where the high-velocity CO emission is present (Pardo et al. 2005). The [C I]  $3P_2-3P_1$  integrated line intensity peaks NE of the Hot Core and also toward Peak 1. The [C I] emission was interpreted as CO dissociation in *J*-shocks. Interestingly, both the OH/H<sub>2</sub>O  $84.6/75.4\mu\text{m}$  map in Fig. 4a as well as the CO  $34-33/21-20$  map in Fig. 5a suggest such a shell structure.

The strong H<sub>2</sub> lines in Orion are usually explained as the signature of non-dissociative shocks (Le Bourlot et al. 2002, and references therein). The high kinetic temperatures that we infer in the *hot* CO component suggest that *significant fraction of hot H<sub>2</sub> and CO coexist*. However, the broad range of inferred H<sub>2</sub> excitation temperatures are not entirely consistent with a single planar *C*-shock that, in a first approximation, can be considered as roughly isothermal at the maximum shock temperature (see Rosenthal et al. 2000).

*C*-type shocks have compression factors ( $n/n_{\text{preshock}} \lesssim 30$ ) smaller than those in *J*-shocks ( $\lesssim 300$ ). Hence, for the same preshock gas density, one could expect the densest shocked gas in *J*-type shocks. Such shocks evolve faster and over smaller spatial scales (e.g., Flower & Pineau Des Forêts 2010). More importantly, given the short dynamical age of the wide-angle outflow ( $< 1000 \text{ yr}$ ) it is very likely that the shock structures have not reached steady state. In this case, shocks in Orion's outflows likely have a range of shock velocities and can show both *C*- and *J*-type

attributes (Chieze et al. 1998; Flower & Pineau des Forêts 2013).

### 6.3. UV-radiation diagnostics: irradiated shocks?

UV-irradiated *C*-shocks have not been previously considered to explain the far-IR emission from Orion but are an alternative solution to interpret the high OH/H<sub>2</sub>O abundance ratios while predicting very high postshock temperatures and bright H<sub>2</sub> lines. C<sup>+</sup>, with an ionization potential of  $11.3 \text{ eV}$ , is the best probe of UV radiation able to dissociate H<sub>2</sub>O, CO and OH molecules. The [C II]  $158\mu\text{m}$  and [O I]  $145\mu\text{m}$  line surface brightness maps observed with *Herschel*/PACS (Figures 1b and 1c) show a similar spatial distribution that is almost orthogonal to that of the H<sub>2</sub> outflow and to the high excitation CO, H<sub>2</sub>O and OH lines. As the [C I]  $3P_2-3P_1$  line (Pardo et al. 2005), [O I] peaks NE of the Hot Core and also shows emission toward the Peak 1 region. They are consistent with molecular gas dissociation.

The spatial distribution of [O I]  $145\mu\text{m}$ /[C II]  $158\mu\text{m}$  line surface brightness ratio, however, is completely different and resembles the plateau, reaching its maximum near Peak 1 (Figure 11). The [O I]  $145\mu\text{m}$ /[C II]  $158\mu\text{m}$  intensity ratio peak value in this region is high,  $\gtrsim 1.4$ , more than a factor 2 higher than the value observed in the Orion Bar PDR (Bernard-Salas et al. 2012). Therefore, the regions shown in Fig. 11 where  $[\text{O I}] 145\mu\text{m}/[\text{C II}] 158\mu\text{m} > 1$  can represent shocks where molecules are dissociated instead of PDR gas at the foreground H II region/OMC1 interfaces.

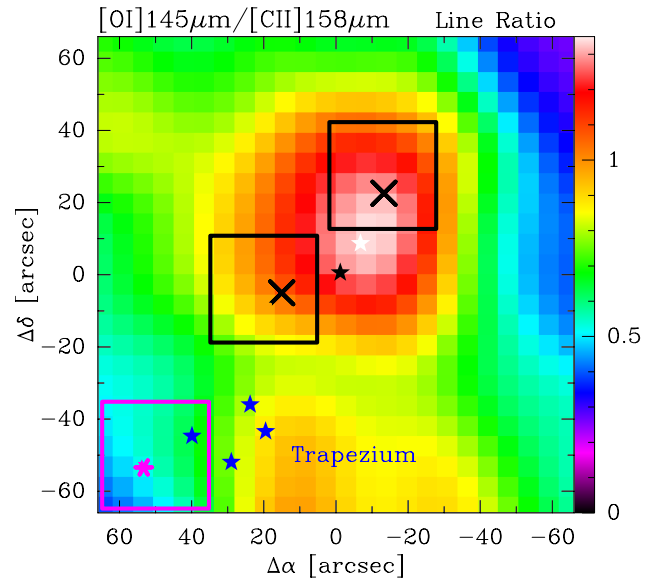


**Figure 11.** Map of the [O I]  $145\mu\text{m}$ /[C II]  $158\mu\text{m}$  surface brightness ratio toward Orion BN/KL outflows obtained from *Herschel*/PACS observations.

Taking into account the FIR dust radiation field toward Peak 1 ( $I_{\text{FIR}} \simeq 0.034 \text{ W m}^{-2} \text{ sr}^{-1}$ ) and assuming that dust grains are heated by UV photons, one can approximately constrain the UV field in the region (e.g., by comparing with the grid of PDR models of Kaufman et al. 1999; Pound & Wolfire 2008). We find that the [O I]  $145\mu\text{m}$ , [C II]  $158\mu\text{m}$  and  $I_{\text{FIR}}$  surface bright-

nesses toward Peak 1 can be reproduced with two possible combinations of gas density and UV field strength ( $G_0$  in Habing's units); A lower density medium with  $n(\text{H}_2) \simeq 10^4 \text{ cm}^{-3}$  and  $G_0 \simeq 5 \times 10^4$  (typical of the foreground PDR between the ionized Orion nebula and OMC1 and thus not related with the star-forming cores) and a higher density medium with  $n(\text{H}_2) \simeq 10^6 \text{ cm}^{-3}$  and  $G_0 \lesssim 100$ . This latter solution is consistent with the gas density in Orion's outflows and would imply that the postshock gas is illuminated by a moderate UV field, also produced *in-situ* by fast  $J$ -shocks (see also Neufeld & Dalgarno 1989b; Haas et al. 1991).

#### 6.4. Is Orion-BN/KL a pathological star forming core?

Early observations of Orion already suggested that there is not enough energy in the H II region or in the protostars embedded in the BN/KL region to provide the observed outflow(s) luminosity. As a consequence, the bright  $\text{H}_2$  and high-velocity CO outflow must have arisen from a cataclysmic explosion (e.g., Kwan & Scoville 1976; Beckwith et al. 1978). Today it is believed that the interaction of sources BN, I and n caused an explosion responsible of the observed wide-angle  $\text{H}_2$  outflow  $\sim 500$ -1000 yr ago (Bally & Zinnecker 2005; Gómez et al. 2005; Zapata et al. 2009; Nissen et al. 2012). In fact, mergers in multiple massive stellar systems may be a common feature in other high-mass star forming regions.

Far-IR observations toward more distant massive-star forming regions can help to disentangle whether Orion BN/KL is more a prototypical or a pathological example. Karska et al. (2014) published PACS spectra toward 10 high-mass star forming sources (from the *WISH* Key Program sample, van Dishoeck et al. 2011) and located at distances ranging from  $\sim 1.5$  to 5 kpc (W33A, W3-IRS5, DR21(OH), NGC 6334-I, G34.26+0.15, etc.). They analyzed the luminosities in the PACS central spaxel ( $\sim 10''$ ) where the far-IR continuum peaks and most of the high- $J$  CO line flux arises ( $\sim 10'' \simeq 0.25 \text{ pc}$  at a distance of 5 kpc). In order to study similar spatial scales, one has to compare with the  $2' \times 2'$  area mapped by us in Orion BN/KL ( $\sim 0.25 \text{ pc} \times 0.25 \text{ pc}$ ) (see the total luminosities in Table 2).

High-mass star-forming regions of the Milky Way's disk observed with *Herschel* show a CO rotational ladder that can be approximately fitted with a single rotational temperature around  $T_{\text{rot}} \simeq 300 \pm 60 \text{ K}$  (line detections typically range from  $J=14$  to 29). This component is similar to the *warm* component inferred toward the Orion Hot Core and  $\text{H}_2$  Peak 1/2 regions from the CO  $J < 30$  lines. The CO  $J=30$ -50 lines, however, are not detected in these more distant regions. This is the range that we associate to a shock-excited *hot* gas component toward Peak 1/2 (with  $T_{\text{rot}}(\text{CO}) \approx 1000 \text{ K}$ ). Since these excited CO lines are detected in the shocks associated with much closer low-mass protostars (e.g., Herczeg et al. 2012; Goicoechea et al. 2012; Manoj et al. 2013) we suspect that their non-detection toward distant high-mass star-forming regions is due to the lack of PACS sensitivity to detect weak lines at short wavelengths.

The far-IR CO lines in the sample of Karska et al. (2014) show an mean absolute luminosity of  $L_{\text{CO}}(\text{PACS}) = 4 \pm 1 L_{\odot}$  if one excludes W51 (G49.5-0.4) (that shows outstanding value of  $L_{\text{CO}}(\text{PACS}) = 25 \pm 11 L_{\odot}$

and  $L_{\text{bol}} \simeq 5 \times 10^5 L_{\odot}$ ). Another extreme luminous massive star forming complex in the disk of the galaxy is W49N (G43.2-0.1), located at a distance of 11.4 kpc and radiating a luminosity of  $L_{\text{bol}} \simeq 10^7 L_{\odot}$  (Ward-Thompson & Robson 1990). Using unpublished *Herschel*/PACS data<sup>13</sup> of W49N we extracted  $L_{\text{CO}}(\text{PACS}) = 70 \pm 11 L_{\odot}$  toward the central spaxel.

In Orion BN/KL, the far-IR CO luminosity in the  $\sim 2' \times 2'$  map is  $L_{\text{CO}}(\text{PACS}) = 64 \pm 10 L_{\odot}$ . Together with W51 and W49N, these 3 high-mass star-forming regions show enhanced CO luminosities compared to other massive regions in the galaxy disk. Nevertheless, the normalized FIR CO luminosity ( $L_{\text{CO}}(\text{PACS})/L_{\text{bol}}$ ) in Orion BN/KL is  $\gtrsim 6 \times 10^{-4}$ , significantly higher than toward any of the above regions (more than an order of magnitude higher than their mean  $5 \times 10^{-5}$  or median  $4 \times 10^{-5}$  values). Despite slightly different evolutionary stages, this suggests that Orion BN/KL is a peculiar protostellar cluster, characterized by violent shocks producing higher  $L_{\text{CO}}/L_{\text{bol}}$  luminosity ratios. This is likely the consequence of a recent explosive event (the merger). The higher probability of protostellar encounters is likely related with the very high stellar density of Orion's core compared with other clusters in the Milky Way (e.g., Rivilla et al. 2013, and references therein).

Regarding water vapor, the observed  $L(\text{H}_2\text{O})/L(\text{CO}) \simeq 0.4$  luminosity ratio toward Peak 1 shows that, overall, CO is more abundant and contributes more to the gas cooling. However, a range of physical conditions and shock velocities likely exist in the shock-excited material that are not resolved by *Herschel*. Our simple models suggest that  $\text{H}_2\text{O}$  is abundant and dominates the gas cooling over CO in the hottest molecular gas. Neufeld et al. (2014) reached similar conclusions after a simultaneous fit of several  $\text{H}_2$ ,  $\text{H}_2\text{O}$  and CO lines toward shocks in the protostellar outflow NGC 2071 and in the supernova remnants W28 and 3C391. As in Orion BN/KL outflows, only fast shocks where the velocity is high enough ( $v_s > 25 \text{ km s}^{-1}$ ) to vaporize the  $\text{H}_2\text{O}$  ice grain mantles Draine (1995) are able to produce copious amounts of water vapor.

## 7. SUMMARY AND CONCLUSIONS

We have presented  $\sim 2' \times 2'$  spectral-maps of Orion BN/KL outflows taken with *Herschel*/PACS. The much improved angular resolution compared to previous far-IR observations allowed us to spatially resolve, for the first time at these critical wavelengths, the intrinsic emission from  $\text{H}_2$  Peaks 1/2 shocks from that of the Hot Core and the ambient cloud. The proximity of Orion makes it a unique laboratory to study the radiative and mechanical feedback induced by massive stars and strong outflows at high spatial resolution. In particular, we obtained the following results:

- Peak 1/2 show a rich pure emission spectrum, with more than 100 lines, most of them rotationally excited lines of  $^{12}\text{CO}$  (up to  $J=48$ -47 with  $E_u/k=6458 \text{ K}$ ),  $\text{H}_2\text{O}$ , OH,  $^{13}\text{CO}$ , and HCN. Around 10% of the observed line emission arises from levels with  $E_u/k > 600 \text{ K}$  for  $\text{H}_2\text{O}$  and  $E_u/k > 2000 \text{ K}$  ( $J > 27$ ) for CO. Bright [O I]  $63,145 \mu\text{m}$  and fainter [C II]  $158 \mu\text{m}$  lines are also detected.

<sup>13</sup> ObsIDs 1342207774 and 1342207775.

- More than half of the far-IR line luminosity toward Peak 1 is provided by CO lines. H<sub>2</sub>O (~20%), OH (~10%) and [O I] (~10%) lines have a less important contribution. Including the mid-IR H<sub>2</sub> ro-vibrational lines and the CO and H<sub>2</sub>O  $v=1-0$  bands, we estimate that ~50% of the total line luminosity is emitted by H<sub>2</sub> followed by CO (~30%) and H<sub>2</sub>O (~10%).
- The CO maps show an evolution of the spatial distribution of the high- $J$  CO lines that has not been reported before. The brightest CO lines are those between  $J=15$  and 20. They show an extended distribution with a half-power radius of ~25'' around the Hot Core. The  $J>30$  lines however, peak toward Peak 1 and show a spatial distribution that resembles the wide-angle H<sub>2</sub> outflow and the high-velocity (low- $J$ ) CO bullets observed from the ground. Better spectral resolution observations are clearly needed to resolve the very excited far-IR CO high-velocity emission.
- Compared to other (sub)mm lines, the far-IR H<sub>2</sub>O and OH lines show a different spatial distribution. Most of them appear in absorption toward the strong far-IR continuum from the Hot Core and IRc sources. The same lines switch to emission toward Peak 1/2. Maps of different line surface brightness ratios suggest an increase of temperature and density toward Peak 1/2.
- The high- $J$  CO and OH lines are a factor  $\approx 2$  brighter toward Peak 1 whereas several excited H<sub>2</sub>O lines are  $\lesssim 50\%$  brighter toward Peak 2. The H<sub>2</sub>O column and the gas density are likely slightly higher towards Peak 2.
- The [O I] 145  $\mu\text{m}$ , [C II] 158  $\mu\text{m}$  and  $I_{\text{FIR}}$  intensities toward Peak 1 can be reproduced with two possible combinations of  $n(\text{H}_2)$  and UV-radiation field. A lower density medium with  $n(\text{H}_2) \simeq 10^4 \text{ cm}^{-3}$  and  $G_0 \simeq 5 \times 10^4$  (typical of the foreground PDRs between the ionized Orion nebula and OMC1) and a higher density medium with  $n(\text{H}_2) \simeq 10^6 \text{ cm}^{-3}$  (similar to the density in the outflows) and  $G_0 \lesssim 100$ . This latter combination would imply that the shocked gas in Orion BN/KL is illuminated by a moderate UV-radiation field, with significant *in-situ* generated UV-photons by fast  $J$ -type shocks.
- From a simple non-LTE model we conclude that most of the CO column density arises from  $T_k \sim 200\text{--}500 \text{ K}$  gas that we associate with low-velocity ( $v_S < 25 \text{ km s}^{-1}$ ) shocks that fail to sputter grain ice mantles and show a maximum gas-phase H<sub>2</sub>O/CO  $\leq 10^{-2}$  abundance ratio. The very excited CO ( $J>35$ ) and H<sub>2</sub>O lines reveal a hotter gas component ( $T_k \sim 2500 \text{ K}$ ) from faster shocks (with a smaller filling factor) that are able to sputter the frozen-out H<sub>2</sub>O and lead to high H<sub>2</sub>O/CO  $\gtrsim 1$  abundance ratios. The moderate H<sub>2</sub>O and high OH luminosities ( $L(\text{H}_2\text{O})/L(\text{CO}) \sim 0.4$  and  $L(\text{OH})/L(\text{H}_2\text{O}) \sim 0.5$ ) cannot be reproduced by shock models that assume high (undepleted) abundances of atomic oxygen in the preshocked gas and/or neglect the presence of UV radiation in the postshock gas (triggering H<sub>2</sub>O photodissociation).
- The *hot* shocked-gas ( $T_k \approx 3500\text{--}1000 \text{ K}$ ) inferred from the CO  $J \gtrsim 35$  lines toward Orion H<sub>2</sub> Peaks is not detected toward the Hot Core nor toward more distant high-mass star-forming regions. The total CO luminosity in these regions (over spatial scales of  $\sim 0.25 \text{ pc}$ ;  $\sim 10''$  at a typical distance of 5 kpc) is usually more than an order of magnitude smaller than  $L(\text{CO})$  over the entire Orion BN/KL region ( $0.25 \text{ pc} \simeq 2'$ ). Prominent

star-forming complexes like W51 or W49N also show comparably high CO luminosities, however, the normalized  $L_{\text{CO}}(\text{PACS})/L_{\text{bol}}$  luminosity toward Orion BN/KL is significantly higher. Orion thus seems more peculiar, probably because its strong outflows and associated shocks were caused by a recent explosive event.

We would like to thank the entire HEXOS GT-KP team for many useful and vivid discussions in the last years. We thank Spanish MINECO for funding support under grants CSD2009-00038, AYA2009-07304 and AYA2012-32032. J.R.G. was supported by a *Ramón y Cajal* contract.

*Facilities:* Herschel Space Observatory

## REFERENCES

- Allen, D. A., & Burton, M. G. 1993, *Nature*, 363, 54  
 Bally, J., & Zinnecker, H. 2005, *AJ*, 129, 2281  
 Bally, J., Cunningham, N. J., Moeckel, N., et al. 2011, *ApJ*, 727, 113  
 Beckwith, S., Persson, S. E., Neugebauer, G., & Becklin, E. E. 1978, *ApJ*, 223, 464  
 Bergin, E. A., Neufeld, D. A., & Melnick, G. J. 1998, *ApJ*, 499, 777  
 Bergin, E. A., & Snell, R. L. 2002, *ApJ*, 581, L105  
 Bergin, E. A., Phillips, T. G., Comito, C., et al. 2010, *A&A*, 521, L20  
 Bernard-Salas, J., Habart, E., Arab, H., et al. 2012, *A&A*, 538, A37  
 Bertoldi, F., Timmermann, R., Rosenthal, D., Drapatz, S., & Wright, C. M. 1999, *A&A*, 346, 267  
 Betz, A. L., & Boreiko, R. T. 1989, *ApJ*, 346, L101  
 Blake, G. A., Sutton, E. C., Masson, C. R., & Phillips, T. G. 1987, *ApJ*, 315, 621  
 Beuther, H., & Nissen, H. D. 2008, *ApJ*, 679, L121  
 Caselli, P., Keto, E., Pagani, L., et al. 2010, *A&A*, 521, L29  
 Caselli, P., Keto, E., Bergin, E. A., et al. 2012, *ApJ*, 759, L37  
 Cernicharo, J., Gonzalez-Alfonso, E., Alcolea, J., Bachiller, R., & John, D. 1994, *ApJ*, 432, L59  
 Cernicharo, J., Pardo, J. R., González-Alfonso, E., et al. 1999, *ApJ*, 520, L131  
 Cernicharo, J., & Crovisier, J. 2005, *Space Sci. Rev.*, 119, 29  
 Cernicharo, J., Goicoechea, J. R., Daniel, F., et al. 2006, *ApJ*, 649, L33  
 Cernicharo, J., 2012, in *ECLA-2011: Proceedings of the European Conference on Laboratory Astrophysics*, European Astronomical Society Publications Series, 2012, Editors : C. Stehl, C. Joblin and L. d'Hendecourt.  
 Chen, J.-H., Goldsmith, P. F., Viti, S., et al. 2014, *ApJ*, in press.  
 Chernoff, D. F., McKee, C. F., & Hollenbach, D. J. 1982, *ApJ*, 259, L97  
 Chieze, J.-P., Pineau des Forets, G., & Flower, D. R. 1998, *MNRAS*, 295, 672  
 De Buizer, J. M., Morris, M. R., Becklin, E. E., et al. 2012, *ApJ*, 749, L23  
 Draine, B. T., & Roberge, W. G. 1982, *ApJ*, 259, L91  
 Draine, B. T., Roberge, W. G., & Dalgarno, A. 1983, *ApJ*, 264, 485  
 Draine, B. T., & McKee, C. F. 1993, *ARA&A*, 31, 373  
 Draine, B. T. 1995, *Ap&SS*, 233, 111  
 Flower, D. R., & Pineau Des Forêts, G. 2010, *MNRAS*, 406, 1745  
 Flower, D. R., & Pineau des Forêts, G. 2013, *MNRAS*, 436, 2143  
 Geballe, T. R., & Garden, R. 1987, *ApJ*, 317, L107  
 Genzel, R., Reid, M. J., Moran, J. M., & Downes, D. 1981, *ApJ*, 244, 884  
 Genzel, R., & Stutzki, J. 1989, *ARA&A*, 27, 41  
 Goicoechea, J. R., Cernicharo, J., Lerate, M. R., et al. 2006, *ApJ*, 641, L49  
 Goicoechea, J. R., Joblin, C., Contursi, A., et al. 2011, *A&A*, 530, L16  
 Goicoechea, J. R., Cernicharo, J., Karska, A., et al. 2012, *A&A*, 548, A77

- Goldsmith, P. F., Melnick, G. J., Bergin, E. A., et al. 2000, *ApJ*, 539, L123
- Goldsmith, P. F., Liseau, R., Bell, T. A., et al. 2011, *ApJ*, 737, 96
- Gómez, L., Rodríguez, L. F., Loinard, L., et al. 2005, *ApJ*, 635, 1166
- Griffin, M. J., Abergel, A., Abreu, A., et al. 2010, *A&A*, 518, L3
- González-Alfonso, E., Wright, C. M., Cernicharo, J., et al. 2002, *A&A*, 386, 1074
- Haas, M. R., Hollenbach, D., & Erickson, E. F. 1991, *ApJ*, 374, 555
- Harwit, M., Neufeld, D. A., Melnick, G. J., & Kaufman, M. J. 1998, *ApJ*, 497, L105
- Hasegawa, T. I., & Herbst, E. 1993, *MNRAS*, 261, 83
- Herczeg, G. J., Karska, A., Bruderer, S., et al. 2012, *A&A*, 540, A84
- Hollenbach, D., & McKee, C. F. 1979, *ApJS*, 41, 555
- Hollenbach, D., & McKee, C. F. 1989, *ApJ*, 342, 306
- Hollenbach, D., Kaufman, M. J., Bergin, E. A., & Melnick, G. J. 2009, *ApJ*, 690, 1497
- Jenkins, E. B. 2009, *ApJ*, 700, 1299
- Johnstone, D., & Bally, J. 1999, *ApJ*, 510, L49
- Karska, A., Herpin, F., Bruderer, S., et al. 2014, *A&A*, 562, A45
- Kaufman, M. J., Wolfire, M. G., Hollenbach, D. J., & Luhman, M. L. 1999, *ApJ*, 527, 795
- Kaufman, M. J., & Neufeld, D. A. 1996, *ApJ*, 456, 611
- Klotz, A., Harju, J., Ristorcelli, I., et al. 2008, *A&A*, 488, 559
- Kwan, J., & Scoville, N. 1976, *ApJ*, 210, L39
- Langer, W. D., & Penzias, A. A. 1990, *ApJ*, 357, 477
- Le Bourlot, J., Pineau des Forêts, G., Flower, D. R., & Cabrit, S. 2002, *MNRAS*, 332, 985
- Lesaffre, P., Chièze, J.-P., Cabrit, S., & Pineau des Forêts, G. 2004, *A&A*, 427, 147
- Lerate, M. R., Barlow, M. J., Swinyard, B. M., et al. 2006, *MNRAS*, 370, 597
- Lu, N., Polehampton, E. T., Swinyard, B. M., et al. 2013, *Experimental Astronomy*, 49
- Manoj, P., Watson, D. M., Neufeld, D. A., et al. 2013, *ApJ*, 763, 83
- Melnick, G. J., Stacey, G. J., Lugten, J. B., Genzel, R., & Poglitsch, A. 1990, *ApJ*, 348, 161
- Melnick, G. J., Ashby, M. L. N., Plume, R., et al. 2000, *ApJ*, 539, L87
- Melnick, G. J., Tolls, V., Neufeld, D. A., et al. 2010, *A&A*, 521, L27
- Melnick, G. J., Tolls, V., Goldsmith, P. F., et al. 2012, *ApJ*, 752, 26
- Menten, K. M., & Reid, M. J. 1995, *ApJ*, 445, L157
- Neufeld, D. A., & Dalgarno, A. 1989, *ApJ*, 340, 869
- Neufeld, D. A., & Dalgarno, A. 1989, *ApJ*, 344, 251
- Neufeld, D. A. 2012, *ApJ*, 749, 125
- Neufeld, D. A., Gusdorf, A., Güsten, R., et al. 2014, *ApJ*, 781, 102
- Nissen, H. D., Cunningham, N. J., Gustafsson, M., et al. 2012, *A&A*, 540, A119
- O'dell, C. R. 2001, *ARA&A*, 39, 99
- Pagani, L., Olofsson, A. O. H., Bergman, P., et al. 2003, *A&A*, 402, L77
- Pardo, J. R., Cernicharo, J., & Phillips, T. G. 2005, *ApJ*, 634, L61
- Peng, T.-C., Zapata, L. A., Wyrowski, F., Güsten, R., & Menten, K. M. 2012a, *A&A*, 544, L19
- Peng, T.-C., Wyrowski, F., Zapata, L. A., Güsten, R., & Menten, K. M. 2012b, *A&A*, 538, A12
- Pilbratt, G. L., Riedinger, J. R., Passvogel, T., et al. 2010, *A&A*, 518, L1
- Poglitsch, A., Waelkens, C., Geis, N., et al. 2010, *A&A*, 518, L2
- Pound, M. W., & Wolfire, M. G. 2008, *Astronomical Data Analysis Software and Systems XVII*, 394, 654
- Rosenthal, D., Bertoldi, F., & Drapatz, S. 2000, *A&A*, 356, 705
- Reid, M. J., Menten, K. M., Greenhill, L. J., & Chandler, C. J. 2007, *ApJ*, 664, 950
- Rivilla, V. M., Martín-Pintado, J., Jiménez-Serra, I., & Rodríguez-Franco, A. 2013, *A&A*, 554, A48
- Rodríguez-Franco, A., Martín-Pintado, J., & Wilson, T. L. 1999, *A&A*, 344, L57
- Rosenthal, D., Bertoldi, F., & Drapatz, S. 2000, *A&A*, 356, 705
- Sempere, M. J., Cernicharo, J., Lefloch, B., González-Alfonso, E., & Leeks, S. 2000, *ApJ*, 530, L123
- Schmid-Burgk, J., Densing, R., Krugel, E., et al. 1989, *A&A*, 215, 150
- Stolovy, S. R., Burton, M. G., Erickson, E. F., et al. 1998, *ApJ*, 492, L151
- Swinyard, B. M., Polehampton, E. T., Hopwood, R., et al. 2014, *MNRAS*, 440, 3658
- Tercero, B., Cernicharo, J., Pardo, J. R., & Goicoechea, J. R. 2010, *A&A*, 517, A96
- van der Werf, P. P., Goss, W. M., & O'Dell, C. R. 2013, *ApJ*, 762, 101
- van Dishoeck, E. F. 2004, *ARA&A*, 42, 119
- van Dishoeck, E. F., Kristensen, L. E., Benz, A. O., et al. 2011, *PASP*, 123, 138
- van Dishoeck, E. F., Herbst, E., & Neufeld, D. A. 2013, *Chemical Reviews*, 113, 9043
- Walmsley, M., Pineau des Forêts, G., & Flower, D. 2005, *Astrochemistry: Recent Successes and Current Challenges*, Proceedings of the 231st Symposium of the IAU. Edited by Lis, Dariusz C.; Blake, Geoffrey A.; Herbst, Eric. Cambridge: Cambridge University Press, 2005., pp.135-140
- Ward-Thompson, D., & Robson, E. I. 1990, *MNRAS*, 244, 458
- Whittet, D. C. B. 2010, *ApJ*, 710, 1009
- Wright, C. M., van Dishoeck, E. F., Black, J. H., et al. 2000, *A&A*, 358, 689
- Zapata, L. A., Schmid-Burgk, J., Ho, P. T. P., Rodríguez, L. F., & Menten, K. M. 2009, *ApJ*, 704, L45
- Zapata, L. A., Loinard, L., Schmid-Burgk, J., et al. 2011, *ApJ*, 726, L12

## APPENDIX

LINE FLUXES TOWARD H<sub>2</sub> PEAK 1

In the next tables we present the observed line fluxes toward Orion Peak 1 in the wavelength range  $\sim 54\text{--}310\,\mu\text{m}$  obtained from *Herschel*/PACS and SPIRE spectra in an aperture of  $\sim 30'' \times 30''$ .

**Table 3**  
CO line fluxes toward Orion Peak 1

Species	Transition	$\lambda(\mu\text{m})$	$E_u/k$ (K)	$F$ ( $\text{W m}^{-2}$ ) <sup>a</sup>
<sup>12</sup> CO	$J=9\text{--}8$	289.12	248.9	6.69E-14
<sup>12</sup> CO	$J=10\text{--}9$	260.24	304.2	9.18E-14
<sup>12</sup> CO	$J=11\text{--}10$	236.613	365.0	1.14E-13
<sup>12</sup> CO	$J=12\text{--}11$	216.927	431.3	1.41E-13
<sup>12</sup> CO	$J=13\text{--}12$	200.272	503.2	1.61E-13
<sup>12</sup> CO	$J=14\text{--}13$	185.999	580.5	1.84E-13
<sup>12</sup> CO	$J=15\text{--}14$	173.631	663.4	2.03E-13
<sup>12</sup> CO	$J=16\text{--}15$	162.812	751.8	2.21E-13
<sup>12</sup> CO	$J=17\text{--}16$	153.267	845.6	2.52E-13
<sup>12</sup> CO	$J=18\text{--}17$	144.784	945.0	2.43E-13
<sup>12</sup> CO	$J=19\text{--}18$	137.196	1049.9	2.27E-13
<sup>12</sup> CO	$J=20\text{--}19$	130.369	1160.3	2.13E-13
<sup>12</sup> CO	$J=21\text{--}20$	124.193	1276.1	2.04E-13
<sup>12</sup> CO	$J=22\text{--}21$	118.581	1397.4	1.80E-13
<sup>12</sup> CO	$J=24\text{--}23$	108.763	1656.6	1.43E-13
<sup>12</sup> CO	$J=28\text{--}27$	93.349	2240.4	6.15E-14
<sup>12</sup> CO	$J=29\text{--}28$	90.163	2399.9	5.73E-14
<sup>12</sup> CO	$J=30\text{--}29$	87.190	2565.0	4.57E-14
<sup>12</sup> CO	$J=32\text{--}31$	81.806	2911.3	3.96E-14
<sup>12</sup> CO	$J=33\text{--}32$	79.360	3092.6	3.37E-14
<sup>12</sup> CO	$J=34\text{--}33$	77.059	3279.3	3.32E-14
<sup>12</sup> CO	$J=35\text{--}34$	74.890	3471.4	2.94E-14
<sup>12</sup> CO	$J=36\text{--}35$	72.843	3669.0	2.06E-14
<sup>12</sup> CO	$J=37\text{--}36$	70.907	3871.9	1.68E-14
<sup>12</sup> CO	$J=39\text{--}38$	67.336	4293.9	7.18E-15
<sup>12</sup> CO	$J=40\text{--}39$	65.686	4512.9	5.84E-15
<sup>12</sup> CO	$J=41\text{--}40$	64.117	4737.3	5.13E-15
<sup>12</sup> CO	$J=42\text{--}41$	62.624	4967.1	4.51E-15
<sup>12</sup> CO	$J=43\text{--}42$	61.201	5202.2	3.57E-15
<sup>12</sup> CO	$J=44\text{--}43$	59.843	5442.6	4.15E-15
<sup>12</sup> CO	$J=45\text{--}44$	58.547	5688.4	3.24E-15
<sup>12</sup> CO	$J=47\text{--}46$	56.122	6195.8	2.48E-15
<sup>12</sup> CO	$J=48\text{--}47$	54.986	6457.5	2.08E-15
<sup>13</sup> CO	$J=9\text{--}8$	302.415	237.9	6.29E-15
<sup>13</sup> CO	$J=10\text{--}9$	272.205	290.8	1.90E-15
<sup>13</sup> CO	$J=11\text{--}10$	247.490	348.9	3.02E-15
<sup>13</sup> CO	$J=12\text{--}11$	226.898	412.4	4.86E-15
<sup>13</sup> CO	$J=13\text{--}12$	209.476	481.0	2.11E-15
<sup>13</sup> CO	$J=14\text{--}13$	194.546	555.0	2.50E-15
<sup>13</sup> CO	$J=15\text{--}14$	181.608	634.2	3.98E-15
<sup>13</sup> CO	$J=16\text{--}15$	170.290	718.7	3.61E-15
<sup>13</sup> CO	$J=17\text{--}16$	160.305	808.5	2.41E-15
<sup>13</sup> CO	$J=18\text{--}17$	151.431	903.5	2.33E-15
<sup>13</sup> CO	$J=19\text{--}18$	143.494	1003.8	2.15E-15

<sup>a</sup>In a  $\sim 30'' \times 30''$  aperture. Flux calibration accuracy up to  $\sim 30\%$ .

**Table 4**  
H<sub>2</sub>O line fluxes toward Orion Peak 1

Species	Transition	$\lambda(\mu\text{m})$	$E_u/k$ (K)	$F$ (W m <sup>-2</sup> ) <sup>a</sup>
<i>o</i> -H <sub>2</sub> O	3 <sub>12</sub> – 3 <sub>03</sub>	273.193	215.2	1.33E-14
<i>o</i> -H <sub>2</sub> O	3 <sub>21</sub> – 3 <sub>12</sub>	257.790	271	1.61E-14
<i>o</i> -H <sub>2</sub> O	5 <sub>23</sub> – 5 <sub>14</sub>	212.526	608.2	3.57E-15
<i>o</i> -H <sub>2</sub> O	2 <sub>21</sub> – 2 <sub>12</sub>	180.488	159.9	3.90E-14
<i>o</i> -H <sub>2</sub> O	2 <sub>12</sub> – 1 <sub>01</sub>	179.527	80.1	8.72E-14
<i>o</i> -H <sub>2</sub> O	3 <sub>03</sub> – 2 <sub>12</sub>	174.626	162.5	8.17E-14
<i>o</i> -H <sub>2</sub> O	5 <sub>32</sub> – 5 <sub>23</sub>	160.504	697.9	5.23E-15
<i>o</i> -H <sub>2</sub> O	5 <sub>23</sub> – 4 <sub>32</sub>	156.266	608.2	blended
<i>o</i> -H <sub>2</sub> O	3 <sub>30</sub> – 3 <sub>21</sub>	136.494	376.4	3.14E-14
<i>o</i> -H <sub>2</sub> O	5 <sub>14</sub> – 5 <sub>05</sub>	134.935	540.5	1.68E-14
<i>o</i> -H <sub>2</sub> O	4 <sub>23</sub> – 4 <sub>14</sub>	132.407	397.9	4.45E-14
<i>o</i> -H <sub>2</sub> O	4 <sub>32</sub> – 4 <sub>23</sub>	121.719	516.1	4.02E-14
<i>o</i> -H <sub>2</sub> O	6 <sub>16</sub> – 5 <sub>05</sub>	82.030	609.3	5.95E-14
<i>o</i> -H <sub>2</sub> O	4 <sub>23</sub> – 3 <sub>12</sub>	78.741	397.9	1.00E-13
<i>o</i> -H <sub>2</sub> O	3 <sub>21</sub> – 2 <sub>12</sub>	75.380	271	1.12E-13
<i>o</i> -H <sub>2</sub> O	3 <sub>03</sub> – 2 <sub>03</sub>	67.269	376.4	1.10E-14
<i>o</i> -H <sub>2</sub> O	3 <sub>30</sub> – 2 <sub>21</sub>	66.437	376.4	3.60E-14
<i>o</i> -H <sub>2</sub> O	7 <sub>16</sub> – 6 <sub>25</sub>	66.092	979	3.39E-15
<i>o</i> -H <sub>2</sub> O	6 <sub>25</sub> – 5 <sub>14</sub>	65.165	761.3	1.10E-14
<i>o</i> -H <sub>2</sub> O	8 <sub>18</sub> – 7 <sub>07</sub>	63.322	1036.5	4.28E-15
<i>o</i> -H <sub>2</sub> O	4 <sub>32</sub> – 3 <sub>21</sub>	58.698	516.1	4.70E-14
<i>p</i> -H <sub>2</sub> O	2 <sub>02</sub> – 1 <sub>11</sub>	303.459	100.8	2.06E-14
<i>p</i> -H <sub>2</sub> O	1 <sub>11</sub> – 0 <sub>00</sub>	269.273	53.4	6.34E-15
<i>p</i> -H <sub>2</sub> O	4 <sub>22</sub> – 4 <sub>13</sub>	248.247	454.4	4.52E-15
<i>p</i> -H <sub>2</sub> O	2 <sub>20</sub> – 2 <sub>11</sub>	243.972	195.9	8.03E-15
<i>p</i> -H <sub>2</sub> O	4 <sub>13</sub> – 4 <sub>04</sub>	187.110	396.4	1.10E-14
<i>p</i> -H <sub>2</sub> O	3 <sub>22</sub> – 3 <sub>13</sub>	156.194	296.8	blended
<i>p</i> -H <sub>2</sub> O	4 <sub>31</sub> – 4 <sub>22</sub>	146.919	552.3	8.96E-15
<i>p</i> -H <sub>2</sub> O	4 <sub>13</sub> – 3 <sub>22</sub>	144.518	396.4	2.43E-14
<i>p</i> -H <sub>2</sub> O	3 <sub>13</sub> – 2 <sub>02</sub>	138.527	204.7	9.14E-14
<i>p</i> -H <sub>2</sub> O	3 <sub>31</sub> – 3 <sub>22</sub>	126.713	410.4	2.01E-14
<i>p</i> -H <sub>2</sub> O	4 <sub>04</sub> – 3 <sub>13</sub>	125.353	319.5	6.24E-14
<i>p</i> -H <sub>2</sub> O	5 <sub>24</sub> – 5 <sub>15</sub>	111.626	598.9	8.91E-15
<i>p</i> -H <sub>2</sub> O	3 <sub>22</sub> – 2 <sub>11</sub>	89.988	296.8	4.79E-14
<i>p</i> -H <sub>2</sub> O	6 <sub>06</sub> – 5 <sub>15</sub>	83.283	642.7	1.84E-14
<i>p</i> -H <sub>2</sub> O	7 <sub>17</sub> – 6 <sub>06</sub>	71.539	843.8	8.48E-15
<i>p</i> -H <sub>2</sub> O	5 <sub>24</sub> – 4 <sub>13</sub>	71.066	598.9	1.08E-14
<i>p</i> -H <sub>2</sub> O	3 <sub>31</sub> – 2 <sub>20</sub>	67.089	410.4	2.87E-14
<i>p</i> -H <sub>2</sub> O	8 <sub>08</sub> – 7 <sub>17</sub>	63.457	1070.6	1.60E-15
<i>p</i> -H <sub>2</sub> O	4 <sub>31</sub> – 4 <sub>04</sub>	61.808	552.3	2.02E-15
<i>p</i> -H <sub>2</sub> O	8 <sub>26</sub> – 7 <sub>35</sub>	60.162	1414.2	4.03E-16
<i>p</i> -H <sub>2</sub> O	7 <sub>26</sub> – 6 <sub>15</sub>	59.986	1021.0	8.02E-16
<i>p</i> -H <sub>2</sub> O	4 <sub>22</sub> – 3 <sub>13</sub>	57.636	454.4	2.37E-14
<i>p</i> -H <sub>2</sub> O	4 <sub>31</sub> – 3 <sub>22</sub>	56.324	552.3	1.53E-14

<sup>a</sup>In a  $\sim 30'' \times 30''$  aperture. Flux calibration accuracy up to  $\sim 30\%$ .



**Table 5**  
OH line fluxes toward Orion Peak 1

Species	Transition	$\lambda(\mu\text{m})$	$E_u/k$ (K)	$F$ (W m <sup>-2</sup> ) <sup>a</sup>
OH	$^2\Pi_{1/2} J = 3/2^- - 1/2^+$	163.396	269.8	4.34E-014
OH	$^2\Pi_{1/2} J = 3/2^+ - 1/2^-$	163.015	270.2	4.34E-014
OH	$^2\Pi_{3/2} J = 5/2^+ - 3/2^-$	119.441	120.5	8.50E-014
OH	$^2\Pi_{3/2} J = 5/2^- - 3/2^+$	119.234	120.8	8.50E-014
OH	$^2\Pi_{3/2} J = 7/2^- - 5/2^+$	84.597	290.5	6.81E-014
OH	$^2\Pi_{3/2} J = 7/2^+ - 5/2^-$	84.420	291.2	blended
OH	$^2\Pi_{1/2} - ^2\Pi_{3/2} J = 1/2^+ - 3/2^-$	79.179	181.7	blended
OH	$^2\Pi_{1/2} - ^2\Pi_{3/2} J = 1/2^- - 3/2^+$	79.116	181.9	1.14E-013
OH	$^2\Pi_{1/2} J = 7/2^+ - 5/2^-$	71.215	617.9	1.38E-014
OH	$^2\Pi_{1/2} J = 7/2^- - 5/2^+$	71.171	617.7	1.38E-014
OH	$^2\Pi_{3/2} J = 9/2^+ - 7/2^-$	65.279	511.0	2.35E-014
OH	$^2\Pi_{3/2} J = 9/2^- - 7/2^+$	65.132	512.1	2.36E-014
OH	$^2\Pi_{1/2} J = 9/2^- - 7/2^+$	55.955	875.1	3.51E-015

<sup>a</sup>In a  $\sim 30'' \times 30''$  aperture. Flux calibration accuracy up to  $\sim 30\%$ .

**Table 6**  
Atomic fine structure line fluxes toward Orion Peak 1

Species	Transition	$\lambda(\mu\text{m})$	$E_u/k$ (K)	$F$ (W m <sup>-2</sup> ) <sup>a</sup>
[C II]	$^2P_{3/2} - ^2P_{1/2}$	157.741	91	6.30E-14
[O I]	$^3P_0 - ^3P_1$	145.525	327	8.68E-14
[O III]	$^3P_1 - ^3P_0$	88.356	163	3.51E-12
[O I]	$^3P_1 - ^3P_2$	63.184	228	5.59E-13
[N III]	$^2P_{3/2} - ^2P_{1/2}$	57.317	251	1.82E-14

<sup>a</sup>In a  $\sim 30'' \times 30''$  aperture. Flux calibration accuracy up to  $\sim 30\%$ .